

# Viscous deformation of geosynthetic reinforcement under cyclic loading conditions and its model simulation

W. Kongkitkul<sup>1</sup>, D. Hirakawa<sup>2</sup>, F. Tatsuoka<sup>3</sup> and T. Uchimura<sup>4</sup>

<sup>1</sup>Graduate student, Department of Civil Engineering, University of Tokyo, 7-3-1 Hongo, Bunkyo-ku, Tokyo 113-8656, Japan, Telephone: +81 3 5841 6123, Telefax: +81 3 5841 8504, E-mail: warat@geot.t.u-tokyo.ac.jp

<sup>2</sup>Research Associate, Faculty of Science and Technology, Tokyo University of Science; formerly graduate student of the University of Tokyo, 2641, Yamazaki, Noda, Chiba 278-8510, Japan, Telephone: +81 4 7124 1501, Telefax: +81 4 7123 9766, E-mail: dhirakaw@rs.noda.tus.ac.jp

<sup>3</sup>Professor, Department of Civil Engineering, Tokyo University of Science, Yamazaki, Noda City, Chiba Prefecture, Japan, Telephone: +81 4 7122 9819, Telefax: +81 4 7123 9766, E-mail: tatsuoka@r.s.noda.tus.ac.jp

<sup>4</sup>Assistant Professor, Department of Civil Engineering, University of Tokyo, 7-3-1 Hongo, Bunkyo-ku, Tokyo 113-8656, Japan, Telephone: +81 3 5841 6124, Telefax: +81 3 5841 8504, E-mail: uchimura@geot.t.u-tokyo.ac.jp

Received 12 September 2003, revised 9 January 2004, accepted 9 January 2004

**ABSTRACT:** To evaluate the deformation characteristics of geosynthetic reinforcement under cyclic loading conditions, a series of tensile loading tests were performed on three types of polymer geogrid and one type of geocomposite using a wide variety of loading histories, including cyclic loading and sustained loading applied during otherwise monotonic loading. In order to separate the loading rate effects due to viscous properties from the rate-independent cyclic loading effects, cyclic loading was applied at five different frequencies for the same total period of cyclic loading at several base loads using two different load amplitudes. It is shown that the residual strain that develops during a given cyclic loading history is controlled essentially by the total period of cyclic loading, whereas it is independent of loading frequency (i.e. independent of the number of loading cycles). That is, the residual strain that develops during a given cyclic loading history is due mostly to the intrinsic viscous properties of the respective geosynthetic reinforcement type. The whole relationship between the tensile load and the tensile strain measured from the start to the end of the respective test, which consisted of monotonic loading and cyclic or sustained loading or both, was successfully simulated by a non-linear three-component rheology model with parameters that do not incorporate any rate-independent cyclic loading effects.

**KEYWORDS:** Geosynthetics, Creep, Cyclic loading, Geocomposite, Geogrid, Non-linear three-component model, Residual strain, Tensile loading test, Viscous properties

**REFERENCE:** Kongkitkul, W., Hirakawa, D., Tatsuoka, F. & Uchimura, T. (2004). Viscous deformation of geosynthetic reinforcement under cyclic loading conditions and its model simulation. *Geosynthetics International*, 11, No. 2, 73–99

## 1. INTRODUCTION

Different types of polymer geosynthetic reinforcement are widely used to reinforce the backfill of a number of different types of permanent soil structure, including soil-retaining walls and bridge abutments. This is due primarily to the proven cost-effectiveness and validated excellent performance of geosynthetic-reinforced soil (GRS) structures (e.g. Tatsuoka and Leshchinsky 1994; Tatsuoka *et al.* 1997). In particular, the performance level of GRS structures under seismic load has been

shown to be equivalent to that of soil structures reinforced with so-called inextensible reinforcement (typically metal strip) (e.g. Bathurst and Alfaro 1997; White and Holtz 1996) or even better when full-height rigid facings are used for GRS structures (Tatsuoka *et al.* 1996, 1997, 1998). However, despite this good performance, polymer geosynthetic reinforcement is often defined as extensible reinforcement, in comparison to metal reinforcement. It is true that GRS retaining walls could be more deformable during construction than soil-retaining walls reinforced with metal reinforcement (e.g.

Christopher *et al.* 1994). It is known that the deformation characteristics of polymer geosynthetic reinforcement are more or less viscous, and the peak strength decreases noticeably with a decrease in the strain rate at failure. These characteristic features have been studied experimentally by various researchers (e.g. Bathurst and Cai 1994; Hirakawa *et al.* 2003; Kongkitkul *et al.* 2002a, 2002b; Leshchinsky *et al.* 1997; Ling *et al.* 1998; Min *et al.* 1995; Moraci and Montanelli 1997). To the best of the authors' knowledge, however, full-scale case studies of unacceptably large long-term residual deformations due to creep deformation of geosynthetic reinforcement, with and without failure, of GRS structures subjected to typical service load conditions have not been reported. Yet it is of great importance to predict the long-term residual deformation of GRS structures accurately, particularly for those that allow a limited amount of deformation, such as soil-retaining walls and bridge abutments supporting high-speed trains. To this end, the residual deformation characteristics of both geosynthetic reinforcement and backfill subjected both to long-term sustained loading and to cyclic loading should be understood.

GRS structures may be subjected not only to sustained load resulting from the self-weight of the structure and external dead load, but also to long-term cyclic load from traffic and short-term intensive seismic load. In general, in addition to 'yielding by the first time increase in the load', the following two factors are considered to be responsible for the development of residual strain in geosynthetic reinforcement subjected to cyclic loading:

- *Loading rate effects caused by material viscous properties.* Hirakawa *et al.* (2003) performed a comprehensive series of monotonic loading tests at different strain rates with and without step changes in the strain rate and sustained loading at intermediate stages using different types of polymer geosynthetic reinforcement. They showed that the current tensile load is essentially a unique function of instantaneous irreversible strain and its rate in the case of monotonic loading for most types of geosynthetic reinforcement tested. They also showed that the ultimate tensile rupture strength of a given type of geosynthetic reinforcement is basically a function of the strain rate at failure irrespective of intermediate loading histories that may include sustained loading. Christensen (1981) showed that the residual strength of geosynthetic reinforcement is insensitive to the previous application of constant stress as long as the time period of constant stress application is not close to the ultimate lifetime for creep rupture. Moreover, Hirakawa *et al.* (2003) showed that a non-linear three-component rheology model, which was originally proposed for geomaterials (soils and rocks) by Di Benedetto *et al.* (2002) and Tatsuoka *et al.* (2002), could rather accurately simulate the load–strain–time relationship of a given type of geosynthetic reinforcement subjected to a wide variety of loading history.
- *Rate-independent effects of cyclic loading.* When this factor is relevant while the viscous effect is negligible, residual strains that develop during a given cyclic loading history are a function of cyclic loading conditions (e.g. cyclic load amplitude and the number of loading cycles). However, they are not controlled by the total period of cyclic loading under cyclic loading conditions that are otherwise the same. More specifically, they are not controlled by the loading frequency for a given number of load cycles and a given load amplitude in the case of uniform cyclic loading.

Previous research on the behaviour of geosynthetic reinforcement under cyclic loading conditions is rather limited. Bathurst and Cai (1994) and Moraci and Montanelli (1997) performed a series of load-controlled cyclic loading tests at several loading frequencies. Ling *et al.* (1998) performed displacement-controlled cyclic loading tests at a constant strain rate of 10%/min. The results from these experiments were analysed assuming that there is an intrinsic relationship between the residual strain and the number of loading cycles with a given load amplitude and a given initial load state for a given geosynthetic type. In these studies, possible effects of load rate or strain rate were not evaluated. Furthermore, the development of residual strain under sustained loading conditions has been studied separately from that performed under cyclic loading conditions. In particular, it seems that the effects of viscous properties on residual strains that develop during a given cyclic loading history were not considered in these previous studies.

The present study extends the previous work by Hirakawa *et al.* (2003) on the viscous properties of polymer geosynthetic reinforcement. A series of load-controlled cyclic and sustained loading tests were performed during otherwise monotonic tensile loading at a constant load rate on four types of geosynthetic reinforcement (three types of geogrid and one type of geocomposite). It is shown in this paper that, at least for the geosynthetic reinforcement types examined in the present study, the residual strain that develops during a given cyclic loading history is due essentially to the intrinsic viscous properties of the respective geosynthetic reinforcement type, and therefore the assumption that the residual strains that develop during a given cyclic loading history are due solely to rate-independent effects of cyclic loading is not appropriate. It is also shown that a non-linear three-component rheology model, which was originally developed to simulate the viscous effects on the stress–strain behaviour of geomaterials (Di Benedetto *et al.* 2002; Tatsuoka *et al.* 2002), can simulate the test results very well. In particular, after necessary modifications were made, the model, which does not incorporate any rate-independent cyclic loading effects on the model parameters, is now able to simulate very well the entire relationship between the tensile load and the tensile strain measured from the start to the end of the respective test including monotonic loading and sustained loading as well as cyclic loading. Kongkitkul

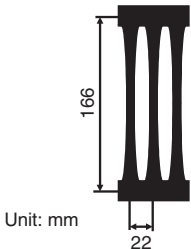
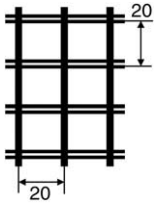
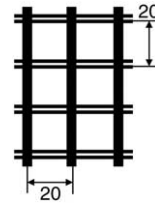
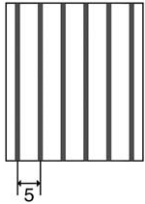
*et al.* (2002a, 2002b) reported some results from this research programme.

## 2. TEST MATERIALS

Three types of geogrid provided by Japanese manufacturers and one type of geocomposite provided by a European manufacturer were used. Hirakawa *et al.* (2003) used these types of geogrid and others in their study. The core fibre material, the coating material, the centre-to-centre spacing between adjacent members and other index properties that are provided by the manufacturers are listed in Table 1. All the specimens were virgin materials, which had been stored in a clean temperature-controlled room to avoid any chemical reaction that might damage them. Each specimen consisted of three longitudinal strands, except for the geocomposite. The geocomposite specimen consisted of six strands so that it could accommodate a pair of displacement transducers on each side. Some more details of these types of geosynthetic reinforcement are presented below:

- *Geogrid A (high-density polyethylene; HDPE)*. This type of geogrid, which is well known by the trademark Tensar, is produced from high-density polyethylene resin. The unidirectional type, designed for use as reinforcement in one direction, was used. The aperture spaces for this geogrid are unique in having a long elliptical shape.
- *Geogrid B (polyarylate)*. This type of geogrid consists of polyarylate and polyester fibres in the longitudinal and transverse directions respectively. The polyarylate fibre (trademark name Vectran) is coated with PVC to protect it from UV light. The centre-to-centre spacing between adjacent members is 20 mm in both the longitudinal and transverse directions. It is one of the major geosynthetic reinforcement types used in the construction of GRS retaining walls in Japan. Kongkitkul *et al.* (2002a, 2002b) reported the time-dependent tensile load and strain relationship of this type of geogrid from displacement-controlled monotonic loading tests with and without sustained and cyclic loading at intermediate stages.
- *Geogrid C (polyvinyl alcohol)*. This type of geogrid consists of polyvinyl alcohol fibres in both the longitudinal and transverse directions (trademark name Vynylon). The polyvinyl alcohol fibres are coated with PVC. Similar to Geogrid B, the centre-to-centre spacing between adjacent members is 20 mm in both longitudinal and transverse directions.
- *Geocomposite D (polyester yarns)*. This type of geocomposite consists of a planar needle-punched nonwoven geotextile made of continuous polypropylene (PP) filament and high-strength polyester (PET) yarns in the longitudinal direction. The centre-to-centre spacing between two parallel adjacent yarns is about 5 mm. The nonwoven geotextile sheet, which has a negligible tensile strength compared with the sheet constructed with PET yarns, is designed only for the drainage function.

**Table 1. Physical and index properties of geosynthetic reinforcements tested in present study**

Reinforcement	A	B	C	D
				
Fibre material: longitudinal Fibre material: transverse	High-density polyethylene High-density polyethylene	Polyarylate Polyester	Polyvinyl alcohol Polyvinyl alcohol	Polyester yarn Nonwoven polypropylene
Coating material	N/A	PVC	PVC	N/A
Nominal tensile strength (kN/m) <sup>(a)</sup> at strain rate of	50.0 1.0%/min	88.0 1.0%/min	60.8 1.0%/min	157.0 20.0%/min
Creep reduction factor <sup>(a)</sup> used in routine design	0.60	0.60	0.60	N/A
No. of strands/yarns	3	3	3	6
No. of cyclic loading stages	2	3	2	3

<sup>(a)</sup> Values provided by the manufacturers.

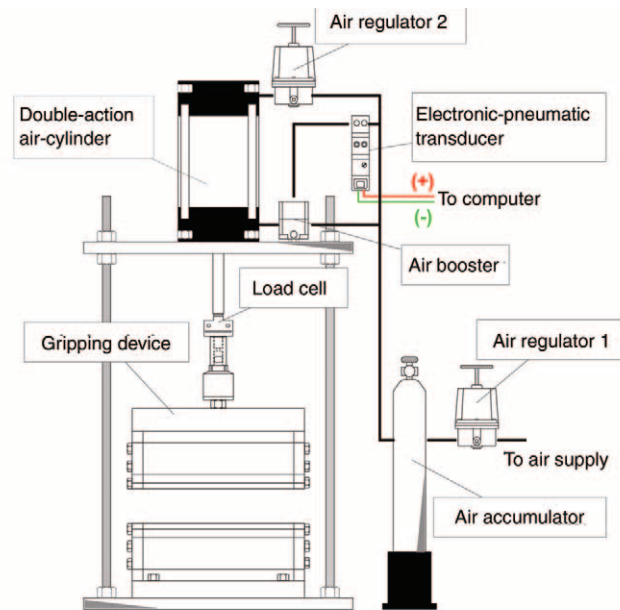
### 3. TEST APPARATUS AND LOADING PATTERNS

#### 3.1. Test apparatus

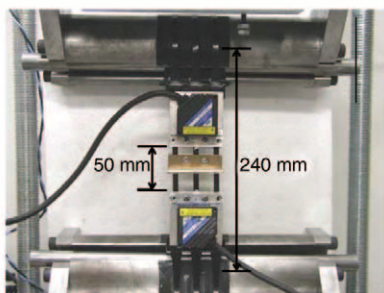
A load-controlled tensile loading apparatus (Figure 1a) with a capacity of about 6 kN was used. Controlled tensile load was provided by means of a double-action air cylinder arranged at the top of a reaction frame. The pressure in the lower chamber of the air cylinder was controlled by using a personal computer through an electro-pneumatic (EP) transducer, and a constant value of air pressure was provided to the upper chamber. To achieve as fast a response as possible during changes in the load rate and direction, the volume of airflow from the electro-pneumatic transducer was amplified by using a volume booster. By using this loading apparatus, cyclic loading tests with a specified load amplitude at a specified frequency were performed, without any intermission at the start of respective cyclic loading, during otherwise monotonic loading at a constant load rate.

The gripping device designed by Hirakawa *et al.* (2003) was used, which consists of a pair of roller clamps. Each clamp consists of a steel cylinder having a smooth surface with a groove prepared to grip a specimen with a small steel rod. A sheet of sandpaper was firmly glued on the surface of the cylinder to prevent any slippage of a wrapped specimen during a test. Excessively high friction can cause the test specimen to rupture at the grips. In the present study, however, rupture did not take place at the grips, but rather between the clamps.

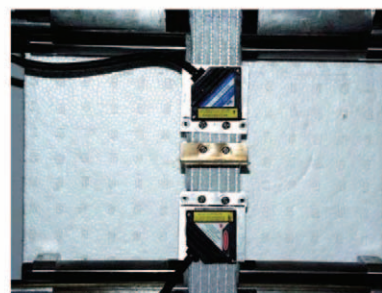
All the geosynthetic reinforcement specimens had a total initial length of about 900 mm with an initial unconfined length of 240 mm. Tensile strains over the central part with an initial gauge length of 50 mm were measured locally by using a pair of laser displacement transducers (Figures 1b and 1c). Specimens of Geogrids A, B and C consisted of three longitudinal strands. In contrast, the specimens of Geocomposite D consisted of a nonwoven geotextile strip with a width of about 30 mm, to which six PET yarns had been sewed. Six



(a)



(b)



(c)

Figure 1. (a) Schematic diagram of load-controlled tensile loading apparatus; (b) a specimen (Geogrid A); (c) a geocomposite specimen (Geocomposite D) (both with a pair of laser displacement transducers to locally measure tensile strains)

**Table 2. Number of cycles per cyclic loading stage at different load rates corresponding to different loading frequencies for a specific loading period of 30 min per stage**

Frequency <sup>(a)</sup> (Hz)	No. of cycles/stage	Load rate during cyclic loading ( $\text{kN m}^{-1} \text{min}^{-1}$ )	
		DA <sup>(b)</sup> = 10 kN/m	DA <sup>(b)</sup> = 20 kN/m
0.01	18	± 12	± 24
0.02	36	± 24	± 48
0.05	90	± 60	± 120
0.1	180	± 120	± 240
0.2	360	± 240	± 480

<sup>(a)</sup> Nominal values. The actual recorded values were slightly different from these values.

<sup>(b)</sup> DA = Double amplitude of cyclic loading.

small holes were punctured through the nonwoven geotextile sheet to accommodate the local strain gauges, as shown in Figure 1c. As the strength of the nonwoven geotextile sheet is much less than that of the six PET yarns, the effects of this procedure were deemed negligible. Each specimen of Geocomposite D with the dimensions described above has a rupture strength much larger than the capacity of the loading device used in the present study. They also exhibited significant necking due to the so-called Poisson's effect in the nonwoven geotextile part when approaching the tensile failure state. Kongkitkul *et al.* (2004a) used specimens consisting of a single yarn attached to a nonwoven geotextile strip with a width of 15 mm that was cut from the original geocomposite to be able to reach the rupture failure. All the tests were conducted at  $25 \pm 2^\circ\text{C}$  in a temperature-controlled laboratory.

### 3.2. Loading paths

The loading scheme was designed assuming that all the geosynthetic reinforcements are installed in the same way in the same structure, which is subjected to the same loading history, consisting of monotonic loading during construction and then cyclic loading during service. Following this scheme, the same tensile load rate ( $60 \text{ kN m}^{-1} \text{min}^{-1}$ ) was employed at all the monotonic loading stages. Also, regardless of the different rupture strengths of the test materials, the same cyclic loading histories, as described in detail below, were applied during otherwise monotonic loading. All the load histories were applied under load-rate-controlled conditions.

Continuous monotonic loading (ML) was applied at a load rate of  $60 \text{ kN m}^{-1} \text{min}^{-1}$  until either of the following two conditions was satisfied:

- The applied load reached the specified level, which was slightly lower than the tensile rupture strength of the respective type of reinforcement so that the laser displacement transducers could be removed safely.
- The applied tensile load reached the capacity of the loading device, about 6 kN (only in the case of Geocomposite D).

Different cyclic loading (CL) histories were applied over a period of 30 min after the tensile load became the respective base load during continuous ML (at a load

rate of  $60 \text{ kN m}^{-1} \text{min}^{-1}$ ), as illustrated in Figures 2a and 2b. Such a CL history as described above was applied either at base loads equal to 10 and 30 kN/m for Geogrids A and C (owing to the limited tensile rupture strengths), or at 10, 30 and 50 kN/m for Geogrid B and Geocomposite D (owing to higher tensile rupture strengths). The load amplitude was 10 kN/m for Geogrid A and Geocomposite D specimens and 10 and 20 kN/m for Geogrids B and C. At each CL stage, positive cyclic loads were added to the respective base tensile load. Cyclic loads were applied at different load rates corresponding to specified different frequencies ( $f$ ) equal to 0.01, 0.02, 0.05, 0.1 and 0.2 Hz for a total period of 30 min (hence, different total numbers of load cycle,  $N_c$ ), as summarised in Table 2. The shape of the cyclic loading time history was therefore sawtoothed and not sinusoidal. The actual recorded frequencies were slightly different from these specified values, whereas the specified numbers of loading cycles were actually applied, as shown later.

Each sustained loading history for a period of 30 min started when the tensile load reached the specified base load (10, 30 or 50 kN/m in one group of tests, and 20, 40 or 60 kN/m in the other group of tests) during continuous ML at a load rate of  $60 \text{ kN m}^{-1} \text{min}^{-1}$  (Figure 3a). These sustained load levels are the same as the maximum and minimum tensile loads during the respective CL history.

Combined sustained and cyclic loading histories were applied at base loads equal to 10, 30 and 50 kN/m for Geogrid B and 10 and 30 kN/m for Geogrid C specimens. As shown in Figure 3b, the total period for each combined loading was 30 min, with the initial sustained loading for 20 min at the base load, followed by CL with a load amplitude of 20 kN/m for 10 min. The cyclic loading frequency was equal to 0.01, 0.05 or 0.2 Hz. This loading scheme was employed to evaluate the effects of creep deformation on the behaviour during subsequent cyclic loading, which would be one of the typical loading histories of prototype structures.

In most of the previous studies (e.g. Bathurst and Cai 1994; Ling *et al.* 1998; Moraci and Montanelli 1997), cyclic tensile loads were applied for a load range between zero tensile load and a specified peak tensile load. In the present study, however, the minimum tensile load during cyclic loading was non-zero. It was considered that this

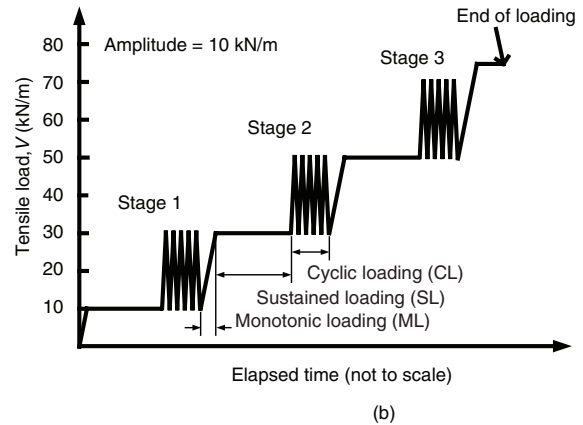
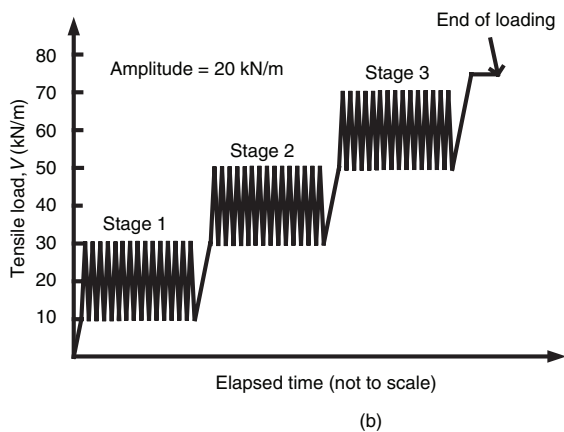
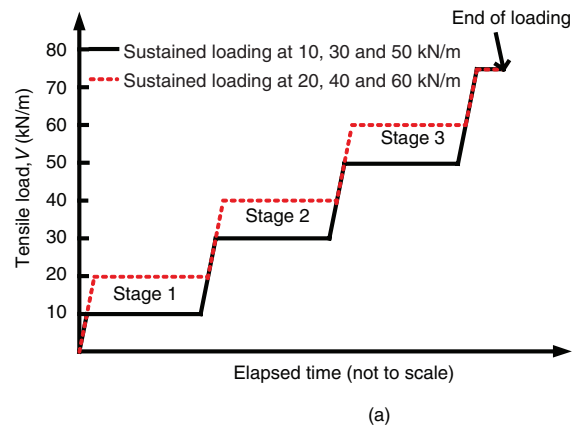
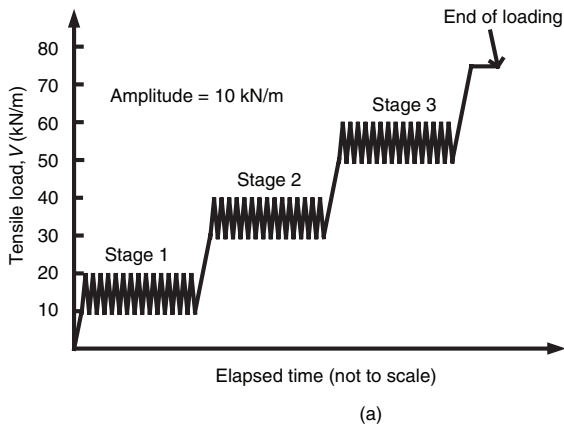


Figure 2. Tensile loading histories for cyclic loading tests with load amplitude of: (a) 10 kN/m; (b) 20 kN/m

Figure 3. Tensile loading histories for: (a) sustained loading tests; (b) combined sustained and cyclic loading, all applied during otherwise ML at constant load rate

difference has minor effects on the intrinsic trend in behaviour during cyclic loading, as essentially the same trend of cyclic behaviour was observed for different cyclic loading amplitudes, as shown below.

## 4. TEST RESULTS AND DISCUSSION

### 4.1. Cyclic deformation characteristics

#### 4.1.1. Load–strain relations

Figures 4a and 4b show the relationships between the tensile load converted to the value for a width of 1 m,  $V$ , and the tensile strain,  $\epsilon$ , from a continuous ML test and two tests including CL stages with a load amplitude of 10 kN/m at  $f = 0.01$  and 0.2 Hz for Geogrid A. Figures 5 to 7 show similar relationships for Geogrids B and C and Geocomposite D, also for a load amplitude of 10 kN/m. Figures 8 and 9 show similar results for Geogrids B and C for a load amplitude of 20 kN/m. The following behaviours can be seen from these figures:

- When ML was restarted from the end of each CL stage, the  $V$ – $\epsilon$  relationship showed a very high tangent stiffness compared with that observed at the same loading level during continuous ML without any intermission of CL. Then, the respective  $V$ – $\epsilon$  curve tended to rejoin the curve during continuous ML without showing any significant effects of previous CL

history on the subsequent load–strain behaviour at higher load levels. This trend of behaviour is essentially similar to that observed upon the restart of ML after sustained loading, as shown later. This fact indicates that cyclic loading has no deleterious effects on the strength and deformation characteristics of geosynthetic reinforcement as well as sustained loading (Hirakawa *et al.* 2003). The same trend in behaviour was also observed in displacement-controlled cyclic loading tests on Geogrid B (Kongkitkul *et al.* 2002a). The trends in behaviour described above can be explained by the viscous properties of geosynthetic reinforcement, as shown below.

- Upon the start of CL at  $f = 0.01$  Hz, the load rate suddenly became lower than 60 kN/m during the original ML by a factor of five for cyclic load amplitude equal to 10 kN/m (Figures 4a, 5a, 6a and 7a), and by a factor of 2.5 for cyclic load amplitude equal to 20 kN/m (Figures 8a and 9a; see also Table 2). Correspondingly, the slope of the  $V$ – $\epsilon$  curve of the initial first half cycle in the respective CL history became noticeably lower than the corresponding one during the original ML. On the other hand, upon the start of CL at  $f = 0.2$  Hz, the load rate suddenly became higher than 60 kN/m during the original ML by a factor of four for cyclic load amplitude equal to 10 kN/m (Figures 4b, 5b, 6b and 7b), and by a factor

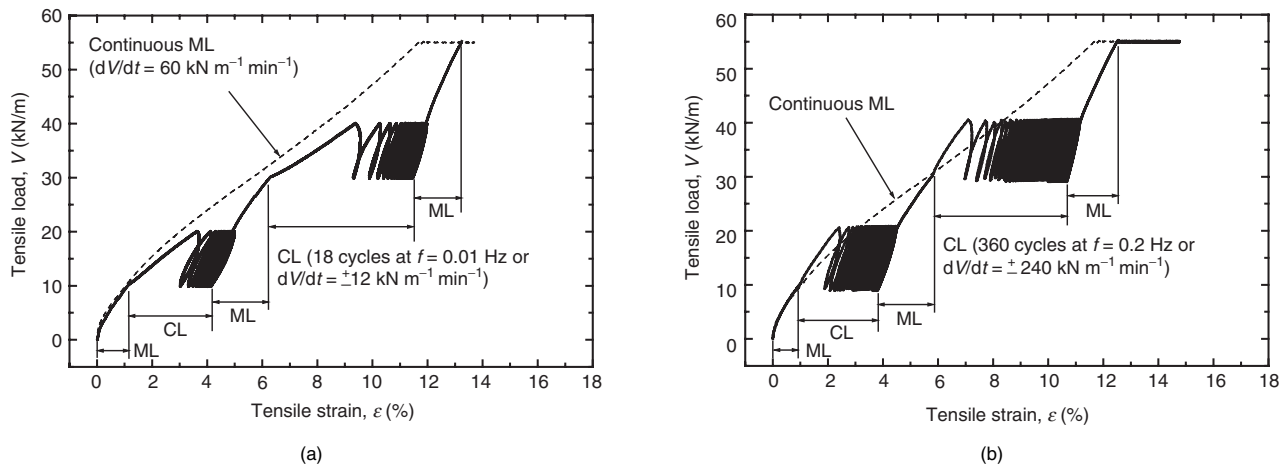


Figure 4. Tensile load–strain relationships for Geogrid A (HDPE) from ML tests at load rate  $dV/dt$  of  $60 \text{ kN m}^{-1} \text{ min}^{-1}$  with and without cyclic loading (CL) at: (a)  $f = 0.01 \text{ Hz}$ ; (b)  $f = 0.2 \text{ Hz}$  with  $10 \text{ kN/m}$  cyclic amplitude

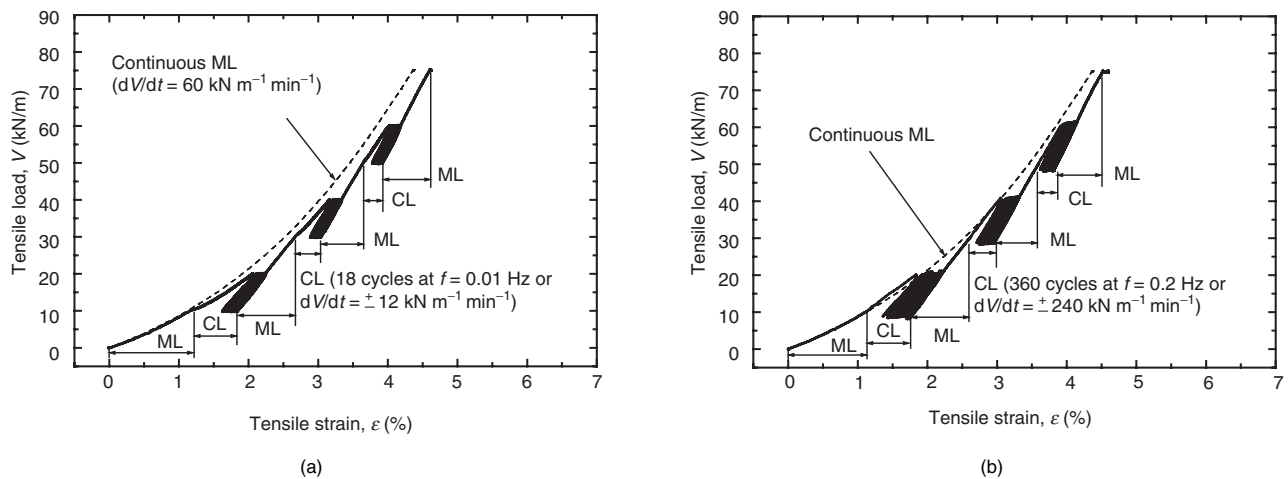


Figure 5. Tensile load–strain relationships for Geogrid B (polyarylate) from ML tests at load rate  $dV/dt$  of  $60 \text{ kN m}^{-1} \text{ min}^{-1}$  with and without cyclic loading (CL) at: (a)  $f = 0.01 \text{ Hz}$ ; (b)  $f = 0.2 \text{ Hz}$  with  $10 \text{ kN/m}$  cyclic amplitude

of eight for cyclic load amplitude equal to  $20 \text{ kN/m}$  (Figures 8b and 9b; see also Table 2). So the slope of the  $V$ - $\varepsilon$  curve of the initial first half cycle in the respective CL history became noticeably larger than the corresponding one during the original ML. This change in the tangent stiffness upon a sudden change in the load rate was due to the loading rate effects caused by viscous properties.

- The development of residual strain was largest during the first half cycle, which was due to the occurrence of large irreversible strain by yielding associated with an increase in the load level exceeding the previous maximum value.
- The residual strain developed by the first cycle of CL increased with a decrease in the loading frequency under otherwise the same conditions. However, for all the tested material types, the total residual strain accumulated for the total period of CL (i.e. 30 min) was rather similar for different frequencies when the cyclic load amplitude was the same. These trends in behaviour can also be explained by material viscous properties, as shown later.

- The residual strain by cyclic loading increased with an increase in the base load for CL with Geogrid A and Geocomposite D, whereas the opposite trend was clearly observed for Geogrid B and slightly for Geogrid C. The latter trend of behaviour is apparently opposite to what might be typically expected. However, the same trend in behaviour was observed with creep strains by Hirakawa *et al.* (2002) and Kongkitkul *et al.* (2002a, 2002b), and also in this study. As shown later, a decrease in the residual strain at cyclic and sustained loading stages with an increase in the load level with Geogrids B and C can be explained by the fact that the tangent stiffness during continuous ML increases with an increase in the load level.

#### 4.1.2. Nature of residual strain development during cyclic loading

In the data plots shown below, the origin for elapsed time is defined at the start of each CL history (point A in Figure 10). This definition is relevant for analysis of the residual deformation of a GRS structure caused by an external additive cyclic vertical load, as due to traffic for example. When necessary for the analysis of deformation

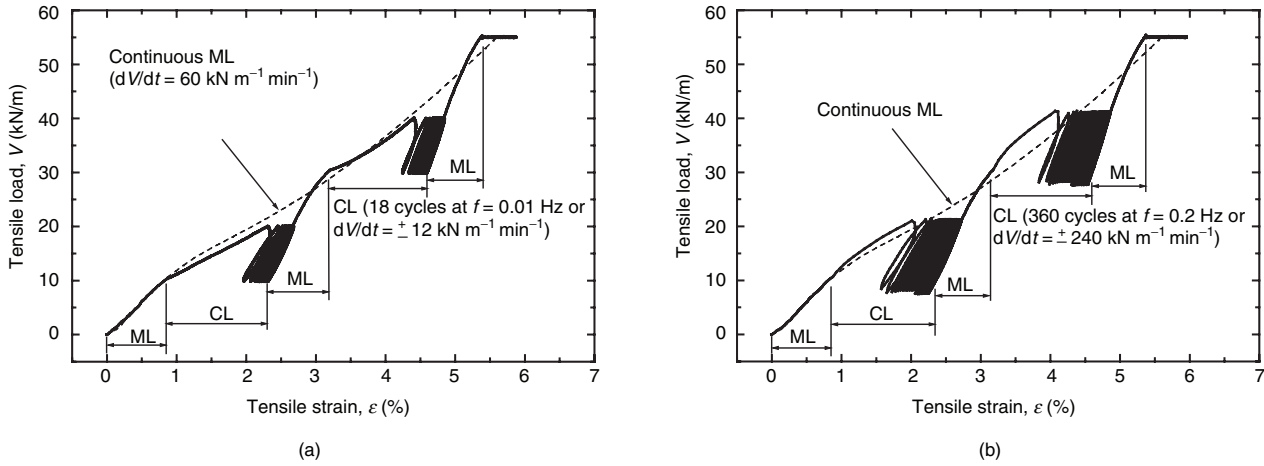


Figure 6. Tensile load–strain relationships for Geogrid C (polyvinyl alcohol) from ML tests at load rate  $dV/dt$  of  $60 \text{ kN m}^{-1} \text{ min}^{-1}$  with and without cyclic loading (CL) at: (a)  $f = 0.01 \text{ Hz}$ ; (b)  $f = 0.2 \text{ Hz}$  with  $10 \text{ kN/m}$  cyclic amplitude

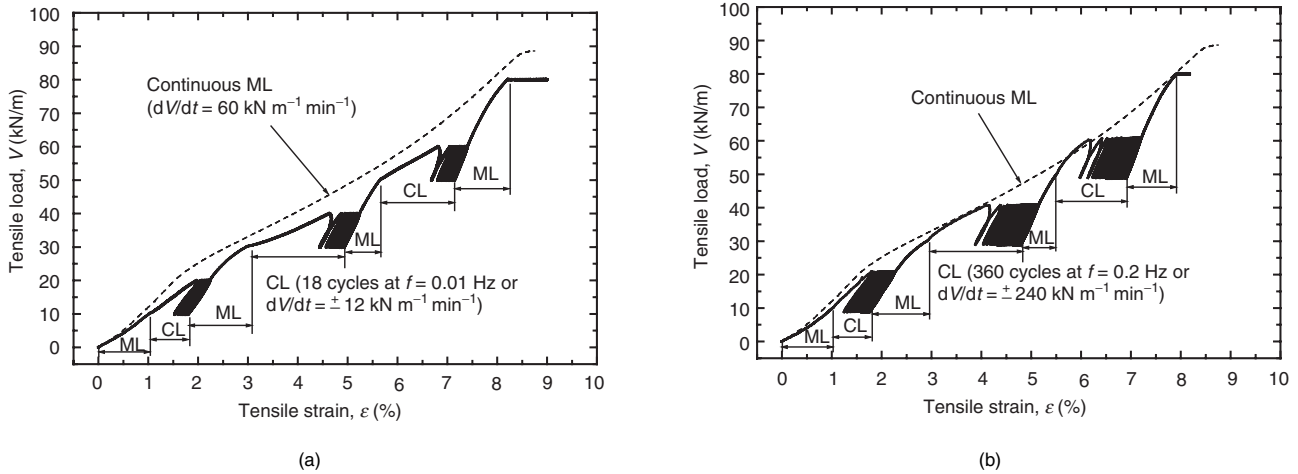


Figure 7. Tensile load–strain relationships for Geocomposite D (polyester yarns) from ML tests at load rate  $dV/dt$  of  $60 \text{ kN m}^{-1} \text{ min}^{-1}$  with and without cyclic loading (CL) at (a)  $f = 0.01 \text{ Hz}$  (b)  $f = 0.2 \text{ Hz}$  with  $10 \text{ kN/m}$  cyclic amplitude

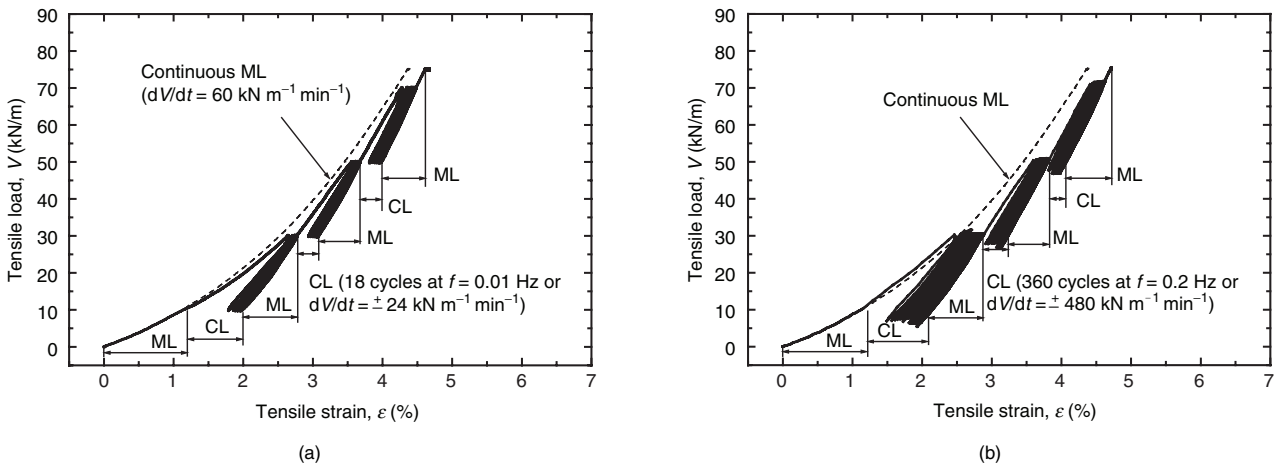
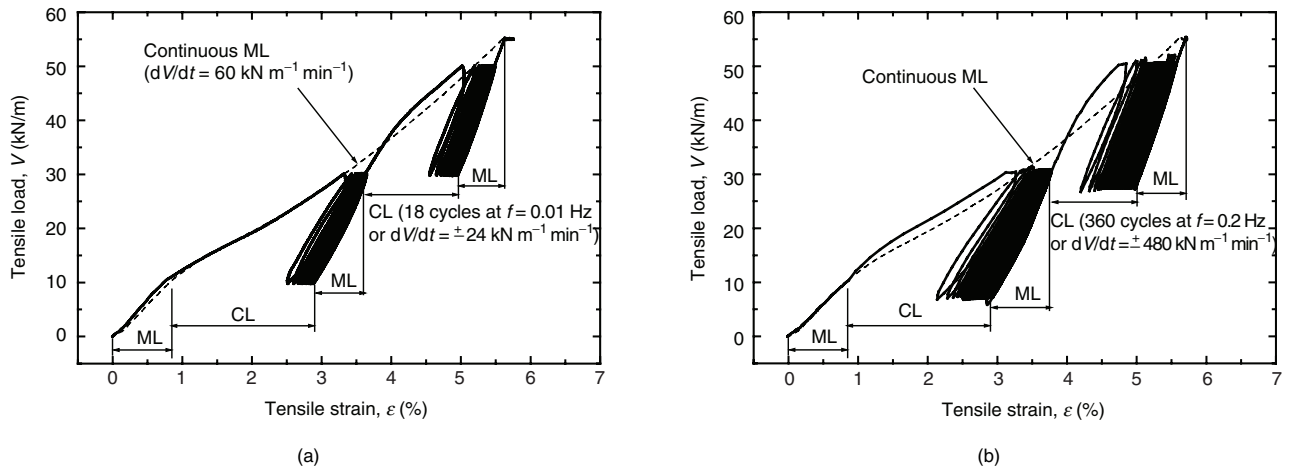


Figure 8. Tensile load–strain relationships for Geogrid B (polyarylate) from ML tests at load rate  $dV/dt$  of  $60 \text{ kN m}^{-1} \text{ min}^{-1}$  with and without cyclic loading (CL) at: (a)  $f = 0.01 \text{ Hz}$ ; (b)  $f = 0.2 \text{ Hz}$  with  $20 \text{ kN/m}$  cyclic amplitude



**Figure 9.** Tensile load–strain relationships for Geogrid C (polyvinyl alcohol) from ML tests at load rate  $dV/dt$  of  $60 \text{ kN m}^{-1} \text{ min}^{-1}$  with and without cyclic loading (CL) at (a)  $f = 0.01 \text{ Hz}$ ; (b)  $f = 0.2 \text{ Hz}$  with  $20 \text{ kN/m}$  cyclic amplitude

by seismic load, the origin of residual strain can be defined at another location, such as point B at the neutral load level of each CL history. Figures 11a and 11b show the time histories of residual strain from the CL tests performed at five different frequencies with a load amplitude of  $10 \text{ kN/m}$  for base loads equal to  $10$  and  $30 \text{ kN/m}$  respectively, for Geogrid A. Each data point in these figures indicates the residual tensile strain observed at the end of the respective cycle when the load became the base load, as shown in Figure 10. Similar results are shown in Figures 12a and 12b (Geogrid B), Figures 13a and 13b (Geogrid C), and Figures 14a and 14b (Geocomposite D). Moreover, the time histories of residual strain of Geogrid B and Geocomposite D at a base load of  $50 \text{ kN/m}$  are plotted in Figures 12c and 14c. Finally, similar results for a load amplitude of  $20 \text{ kN/m}$  are shown in Figure 15 (Geogrid B) and Figure 16 (Geogrid C). The following trends can be observed from these figures:

- In each figure, the time histories of residual tensile strain from CL histories at different loading frequen-

cies in the range  $0.01\text{--}0.2 \text{ Hz}$  under otherwise the same loading conditions are rather similar. When the residual strain is plotted against the number of loading cycles,  $N_c$ , the relationships between the residual

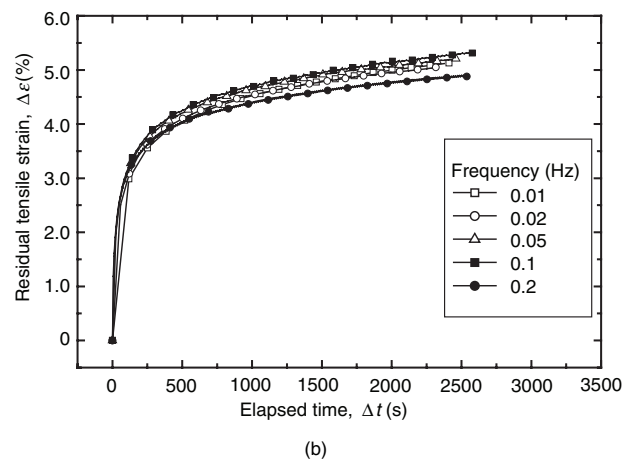
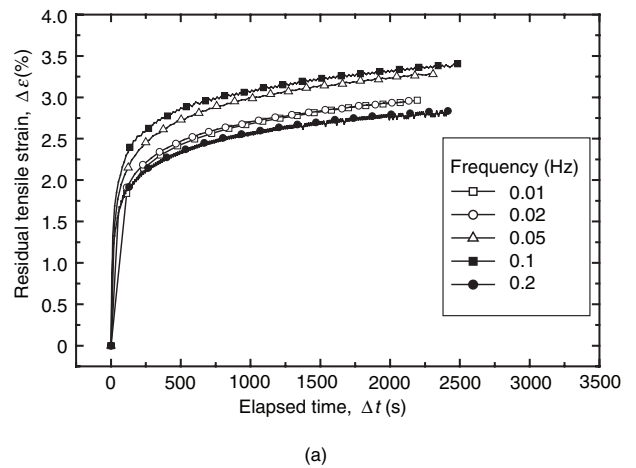


**Figure 11.** Time histories for Geogrid A (HDPE) of residual strain accumulating at base loads of: (a)  $10\text{--}20 \text{ kN/m}$ ; (b)  $30\text{--}40 \text{ kN/m}$  from cyclic loading at  $f = 0.01\text{--}0.2 \text{ Hz}$  for amplitude of  $10 \text{ kN/m}$

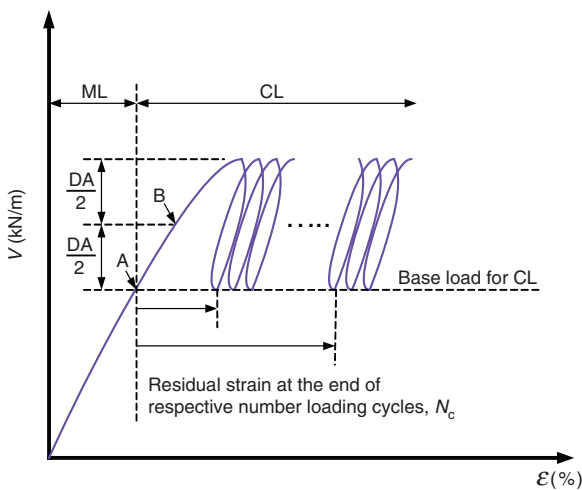
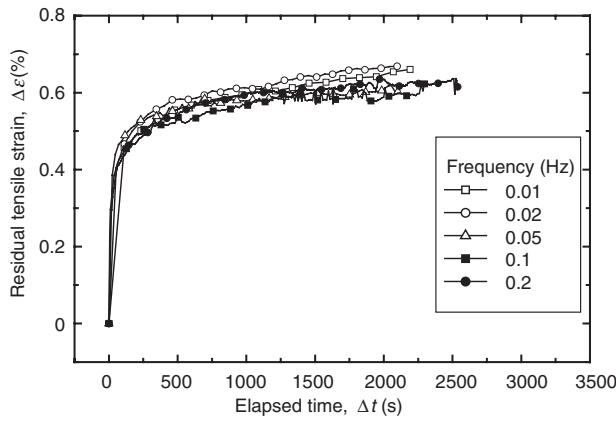
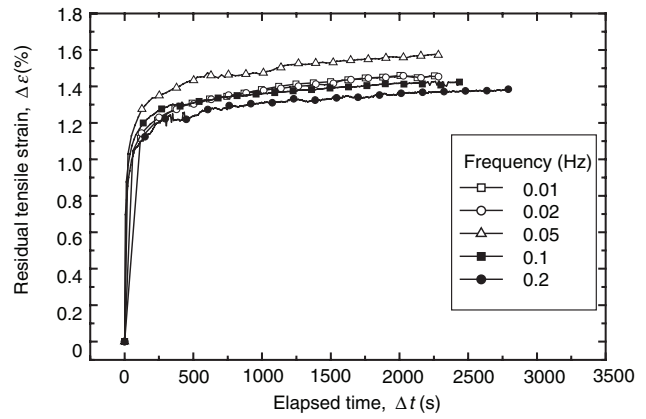


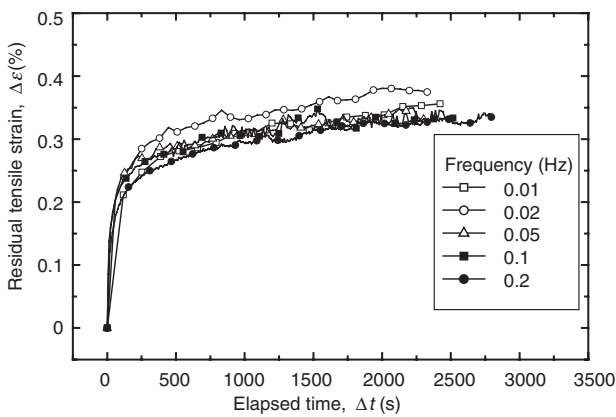
**Figure 10.** Definitions of residual strain during cyclic loading and its origin



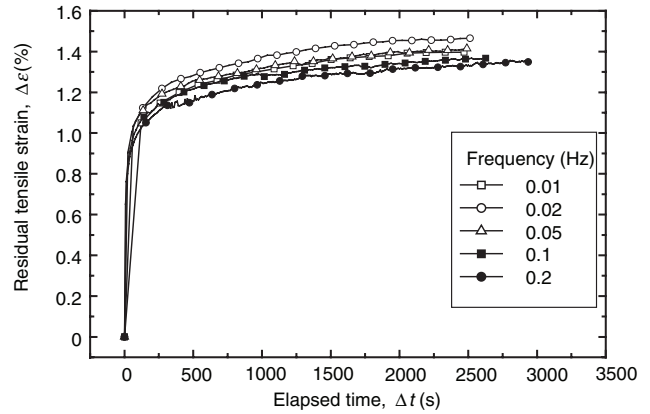
(a)



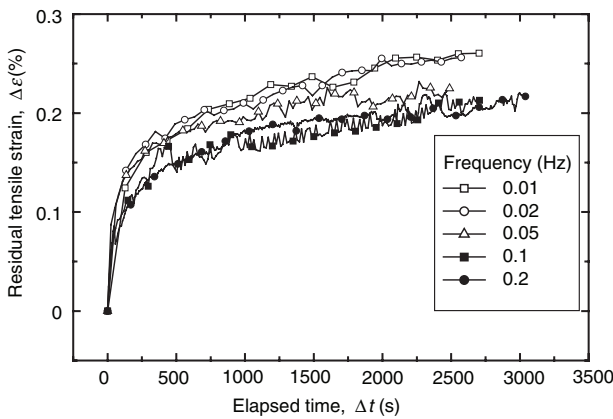
(a)



(b)



(b)



(c)

**Figure 12. Time histories for Geogrid B (polyarylate) of residual strain accumulating at base loads of: (a) 10–20 kN/m; (b) 30–40 kN/m; (c) 50–60 kN/m from cyclic loading at  $f = 0.01$ – $0.2$  Hz for amplitude of 10 kN/m**

tensile strain and  $N_c$  no longer coincide. This fact suggests that the development of residual strain during these CL tests was due essentially to the loading rate effects caused by the material viscous properties.

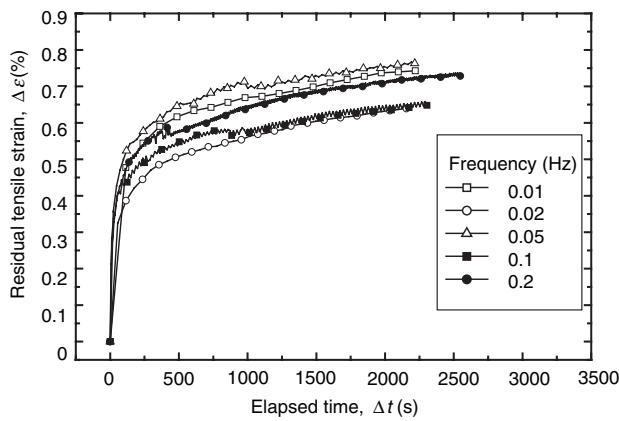
- All the time histories are asymptotic to the respective upper bound curve, and the pattern is nearly the same for different loading frequencies. This trend in behav-

**Figure 13. Time histories for Geogrid C (polyvinyl alcohol) of residual strain accumulating at base loads of: (a) 10–20 kN/m; (b) 30–40 kN/m from cyclic loading at  $f = 0.01$ – $0.2$  Hz for amplitude of 10 kN/m**

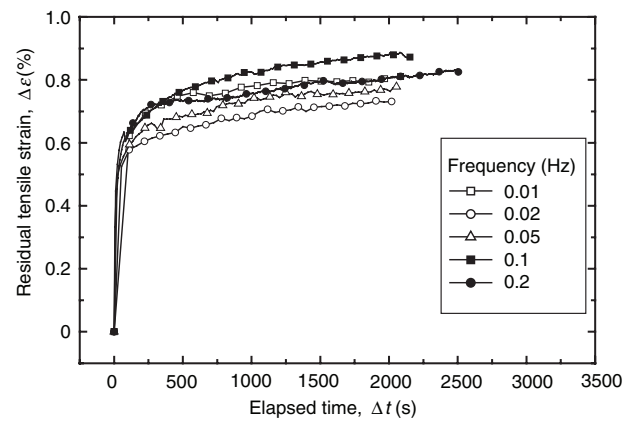
our is essentially the same as the time histories for creep strain, as shown by Hirakawa *et al.* (2003) and also shown below. It is seen from the above discussion that the basic feature of cyclic straining is essentially the same as that of creep deformation. Hirakawa *et al.* (2003) showed that creep deformation of geosynthetic reinforcement is not a degrading phenomenon but merely a viscous response. The fact shown above suggests that this is also the case with residual strains that develop during CL histories.

These two points above are examined more in detail below.

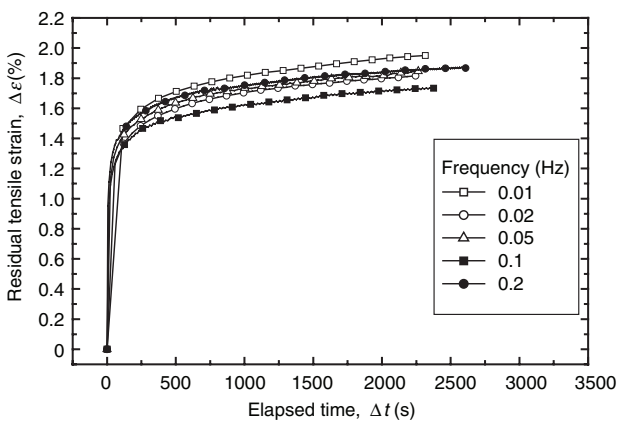
Figure 17 is a schematic diagram showing the relationship between the residual tensile strains at an elapsed time equal to 1000 s,  $(\Delta\epsilon)_{t=1000\text{ s}}$ , and those at a number of loading cycles equal to 10,  $(\Delta\epsilon)_{N_c=10}$ , from a set of CL tests performed at different loading frequencies under otherwise the same test conditions. Note that 1000 s is the duration of 10 cycles at  $f = 0.01$  Hz. The origin for the residual strain at the tenth cycle during each CL history was defined at the start of CL (point A in Figure 10). The following two extreme cases are illustrated in this figure:



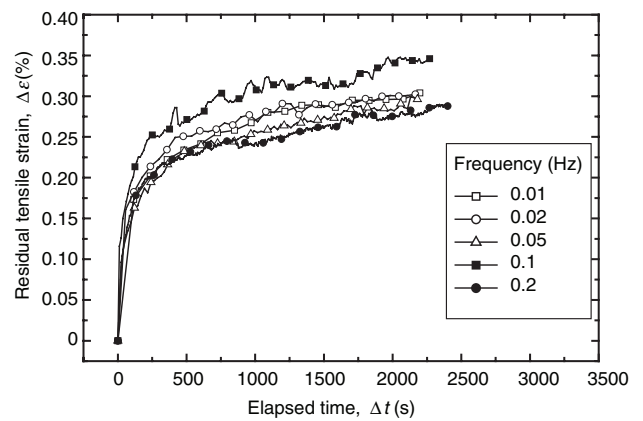
(a)



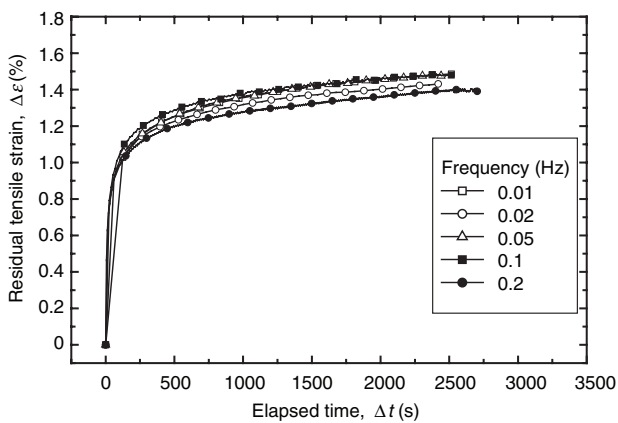
(a)



(b)



(b)



(c)

**Figure 14.** Time histories for Geocomposite D (polyester yarns) of residual strain accumulating at base loads of: (a) 10–20 kN/m; (b) 30–40 kN/m; (c) 50–60 kN/m from cyclic loading at  $f = 0.01\text{--}0.2$  Hz for amplitude of 10 kN/m

- The development of residual tensile strain during a given cyclic loading history is due solely to the viscous properties of the specimen. In this case, the values of  $(\Delta\varepsilon)_{t=1000\text{ s}}$  for different loading frequencies are essentially the same. On the other hand, as the time that is necessary for 10 loading cycles decreases with an increase in the loading frequency, the value of

**Figure 15.** Time histories for Geogrid B (polyarylate) of residual strain accumulating at base loads of: (a) 10–30 kN/m; (b) 30–50 kN/m from cyclic loading at  $f = 0.01\text{--}0.2$  Hz for amplitude of 20 kN/m

$(\Delta\varepsilon)_{N_c=10}$  decreases with an increase in the loading frequency.

- The development of residual tensile strain during a given cyclic loading history is due solely to the rate-independent effect of cyclic loading. In this case, the values of  $(\Delta\varepsilon)_{N_c=10}$  for different loading frequencies are the same, independent of the time that elapses by the end of the tenth cycles. On the other hand, as the total number of loading cycles for a fixed period of time equal to 1000 s increases with an increase in the loading frequency, the value of  $(\Delta\varepsilon)_{t=1000\text{ s}}$  increases with an increase in the loading frequency.

In the figures that follow, the experimental observations are compared with Figure 17 to determine which behaviour is relevant to the various types of geosynthetic reinforcement tested in the present study.

Figures 18a, 18b and 18c summarise such relationships as described above for all the test materials for a cyclic load amplitude of 10 kN/m, and Figure 19 shows the results for Geogrid B and C specimens at a cyclic load amplitude of 20 kN/m. It may be seen from these figures that, although there is some scatter in the data, the first case above is relevant to all the tests performed in the present study: that is, the development of residual tensile

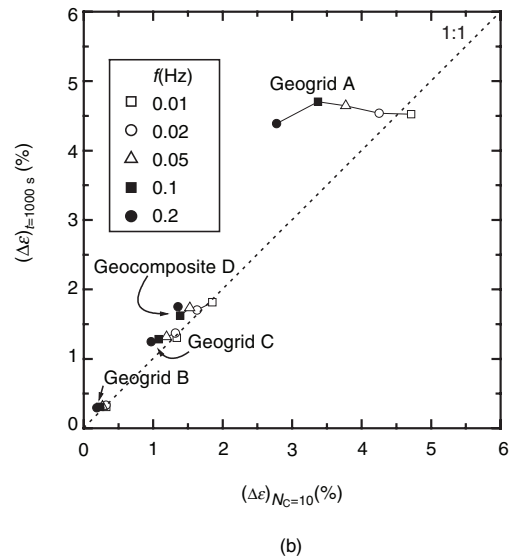
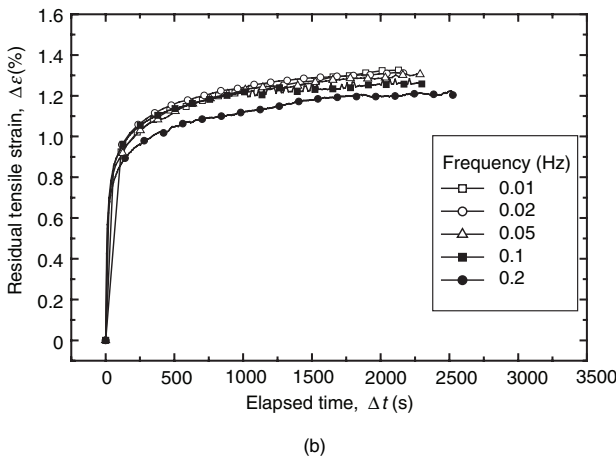
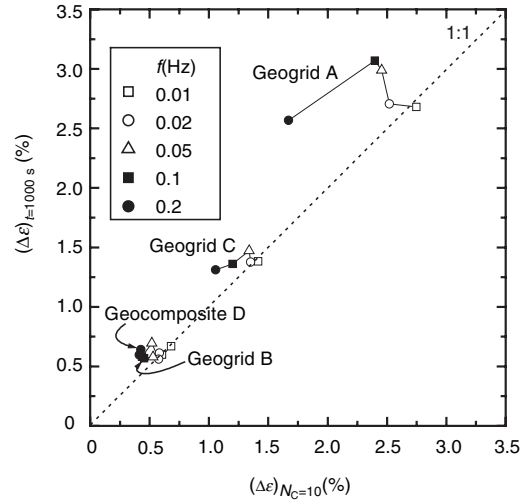
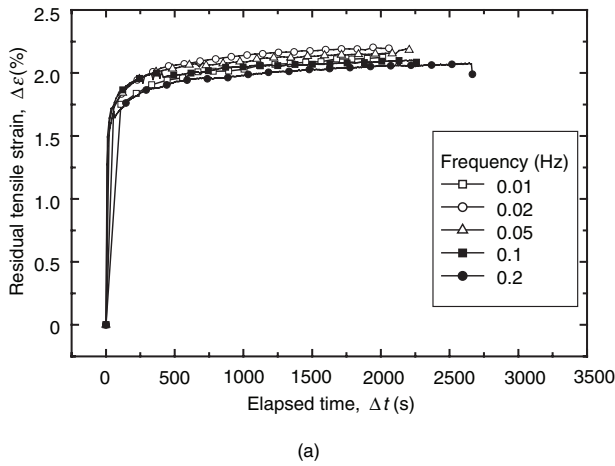


Figure 16. Time histories for Geogrid C (polyvinyl alcohol) of residual strain accumulating at base loads of: (a) 10–30 kN/m; (b) 30–50 kN/m from cyclic loading at  $f = 0.01\text{--}0.2$  Hz for amplitude of 20 kN/m

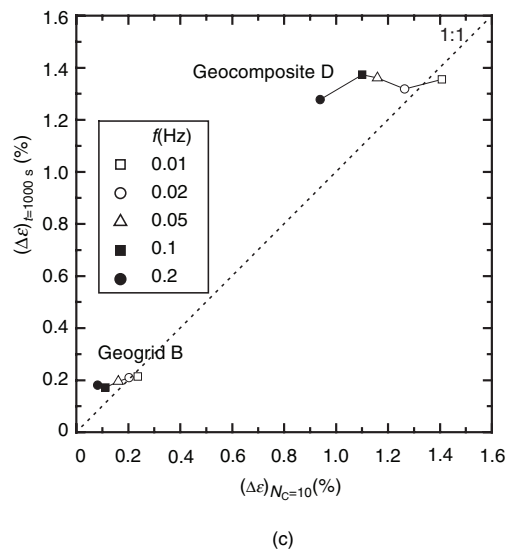
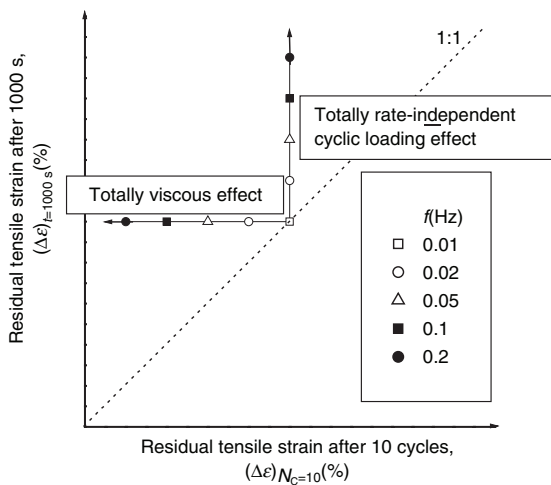
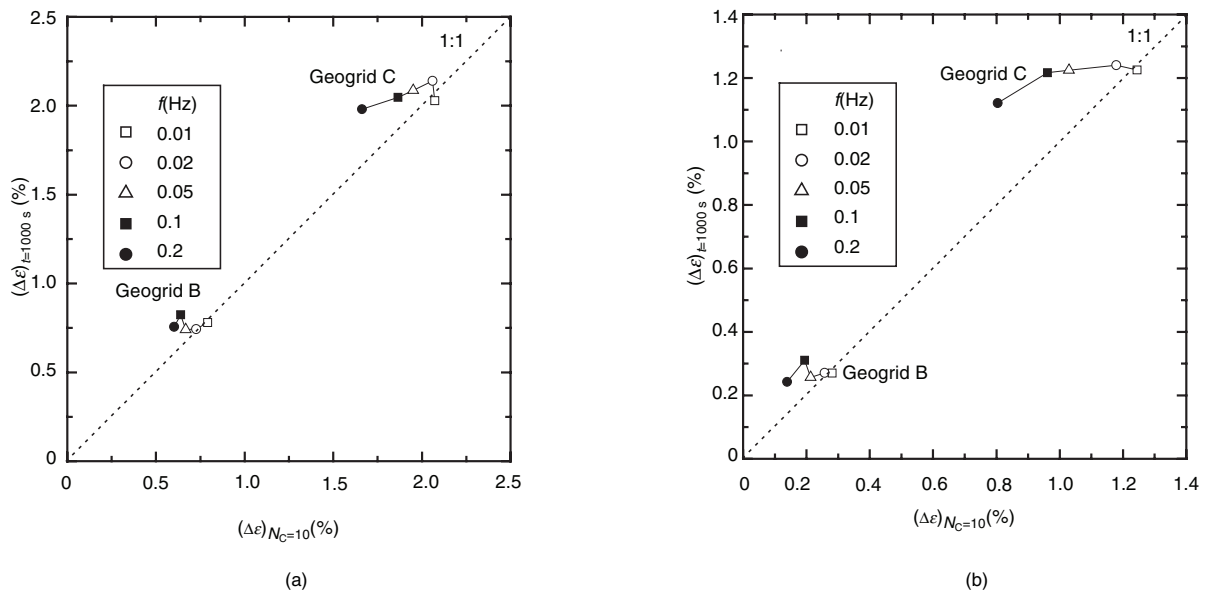


Figure 17. Schematic diagram illustrating the difference in residual strain during cyclic loading between totally viscous effect (horizontal line) and totally rate-independent cyclic loading effect (vertical line)

Figure 18. Relationship between residual tensile strains at elapsed time = 1000 s and number of cycles = 10 from cyclic loading tests at different loading frequencies on four types of geosynthetic reinforcement: (a)  $V = 10\text{--}20$  kN/m; (b)  $V = 30\text{--}40$  kN/m; (c)  $V = 50\text{--}60$  kN/m (all test materials)



**Figure 19. Relationship between residual tensile strains at elapsed time = 1000 s and number of cycles = 10 from cyclic loading tests at different loading frequencies on two types of geosynthetic reinforcement (Geogrids B and C): (a)  $V = 10\text{--}30$  kN/m; (b)  $V = 30\text{--}50$  kN/m**

strain during a given cyclic loading history is essentially a viscous response, in addition to ‘the first time increase in the load’, but rate-independent cyclic loading effects, if any, are negligible. Later in this paper this fact is re-confirmed by a successful simulation of these test results by a non-linear three-component model having model parameters that are constant during a given cyclic loading history.

**4.2. Relationship between residual strains developing during sustained and cyclic loading histories**

It is indicated above that the nature of residual strain that develops during cyclic loading is essentially the same as that of creep strain. This point is examined further in this section. Full-scale structures in the field may be subjected to cyclic loading (such as seismic and traffic

loads) after some period of sustained loading during service. Considering the above, six tests were performed in which initially sustained loading (SL) for 20 min, followed by cyclic loading (CL) at a frequency of 0.01, 0.05 or 0.2 Hz with a load amplitude of 20 kN/m for 10 min was applied at base loads of 10, 30 and 50 kN/m (Geogrid B) or 10 and 30 kN/m (Geogrid C) (see Figure 3b for the loading histories). Figures 20a and 20b show the test results for the cases with  $f = 0.01$  and 0.2 Hz respectively for Geogrid B, and Figures 21a and 21b show the test results for the cases with  $f = 0.01$  and 0.2 Hz respectively for Geogrid C. The other test conditions were the same as for the tests described in Figures 8 and 9. It may be seen from Figures 20 and 21 that the effects of the initial sustained loading have disappeared by the end of the first half cycle of the

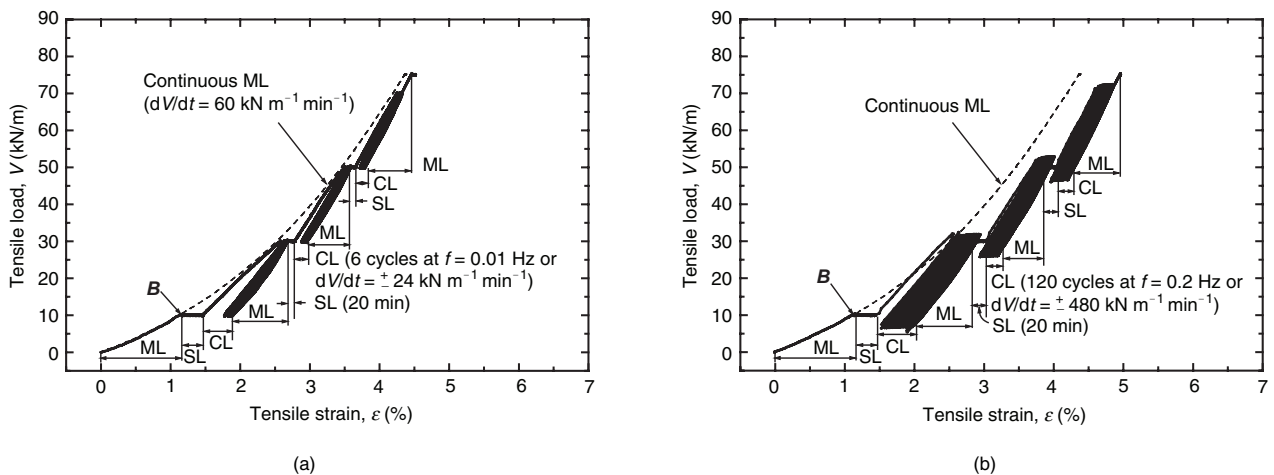


**Figure 20. Tensile load–strain relationships for Geogrid B (polyarylate) from ML tests at load rate  $dV/dt$  of  $60\text{ kN m}^{-1}\text{ min}^{-1}$  with and without initial sustained loading (SL) and cyclic loading (CL) at: (a)  $f = 0.01$  Hz; (b)  $f = 0.2$  Hz with 20 kN/m cyclic amplitude**

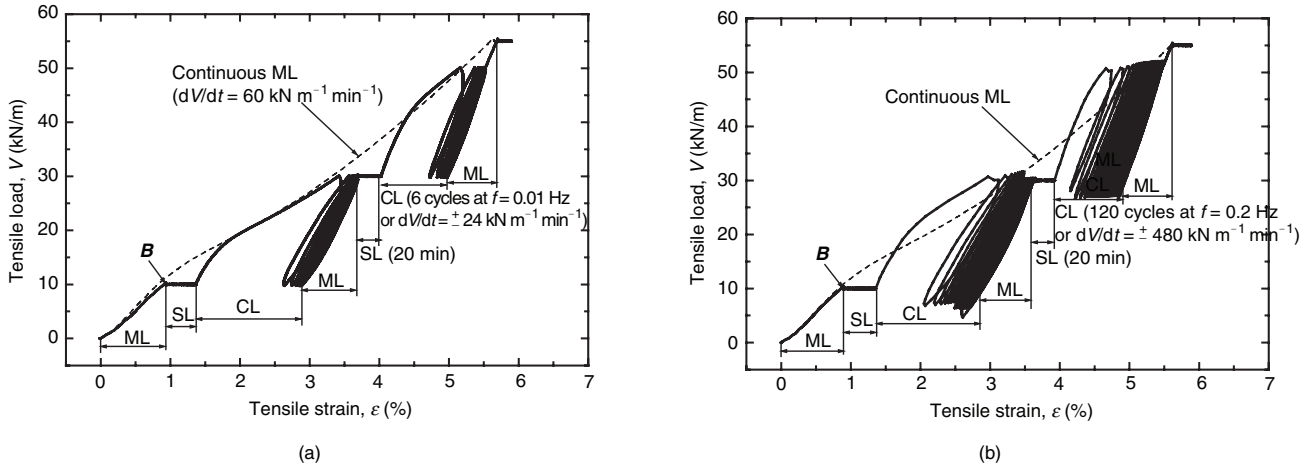


**Figure 21.** Tensile load–strain relationships for Geogrid C (polyvinyl alcohol) from ML tests at load rate  $dV/dt$  of  $60 \text{ kN m}^{-1} \text{ min}^{-1}$  with and without initial sustained loading (SL) and cyclic loading (CL) at: (a)  $f = 0.01 \text{ Hz}$ ; (b)  $f = 0.2 \text{ Hz}$  with  $20 \text{ kN/m}$  cyclic amplitude

following cyclic loading history. Figure 22 compares the relationships between the following two types of residual strain obtained under otherwise the same test conditions from these and other similar tests:

- The residual strain at the end of the first 10 min (or 600 s) obtained from the cyclic loading tests performed directly following the ML history shown in Figures 8 and 9 and other similar tests. The origin is defined at the start of CL (point A in Figure 10).
- The residual strain at the end of cyclic loading (for 10 min) obtained from the tests described in Figures 20 and 21 and other similar tests. The origin of residual strain is defined at the start of the preceding sustained loading history (point B in Figures 20 and 21). It may be seen that the total residual strains from the two types of test (with and without an initial sustained loading phase before the start of cyclic loading) performed under otherwise the same conditions are essentially the same. This fact confirms that the

residual strains developing during sustained loading and cyclic loading are essentially of the same nature.

To reconfirm the above, the developments of residual tensile strain during cyclic and sustained loading histories under otherwise the same test conditions are compared below. Figures 23a to 23d show, respectively, the relationships between the tensile load per unit width ( $V$ ) and the tensile strain ( $\epsilon$ ) obtained from a continuous ML test and two or three other ML tests with sustained loading at multiple intermediate stages (for 30 min each) for the four types of geosynthetic reinforcement tested. It may be seen that, similarly to the test results presented in Figures 4 to 9, upon the restart of ML at a constant load rate after a sustained loading stage, the  $V$ – $\epsilon$  relation showed a higher tangent stiffness than that observed at the same load level during continuous ML. The  $V$ – $\epsilon$  relation then tended to rejoin the original curve observed during continuous ML when the tensile load became sufficiently higher than the sustained load level. This behaviour obviously shows that creep deformation is not a degradation phenomenon, but simply a viscous response of geosynthetic reinforcement.

Figure 24 compares the  $V$ – $\epsilon$  relations from a continuous ML test, from two ML tests with multiple sustained loading stages, and from another with two cyclic loading stages using a cyclic load amplitude of  $10 \text{ kN/m}$  for Geogrid A. To simplify comparison, the sustained loading tests were performed at the minimum load,  $V_0$ , and the maximum load,  $V_0 + \Delta V$ , during the respective CL history (i.e. 10 and 20 kN/m, and 30 and 40 kN/m). The loading frequency,  $f$ , during CL was  $0.05 \text{ Hz}$ , which made the load rate  $\pm 60 \text{ kN m}^{-1} \text{ min}^{-1}$  as during ML. Figures 25a and 25b compare the time histories of residual strain from the CL test and two sustained loading tests for the same base load,  $10 \text{ kN/m}$  and  $30 \text{ kN/m}$ . The origins for residual strain and time for the plots shown in Figures 25a and 25b are defined at point C in Figure 24 (where  $V = 10 \text{ kN/m}$ ) and at point D (where  $V = 30 \text{ kN/m}$ ) respectively. It may be seen

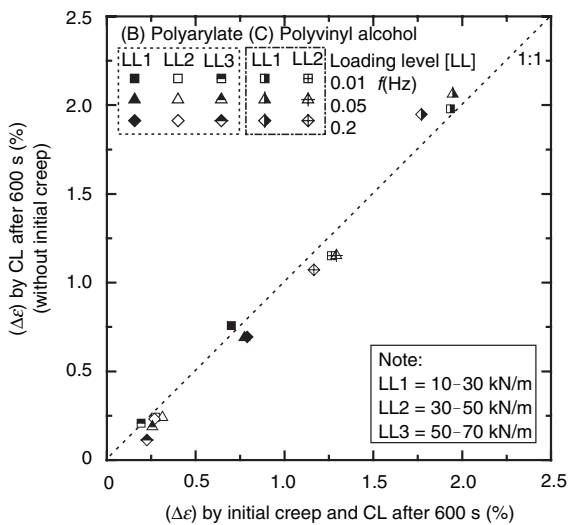


**Figure 22.** Comparison between residual strains from cyclic loading tests with and without initial sustained loading

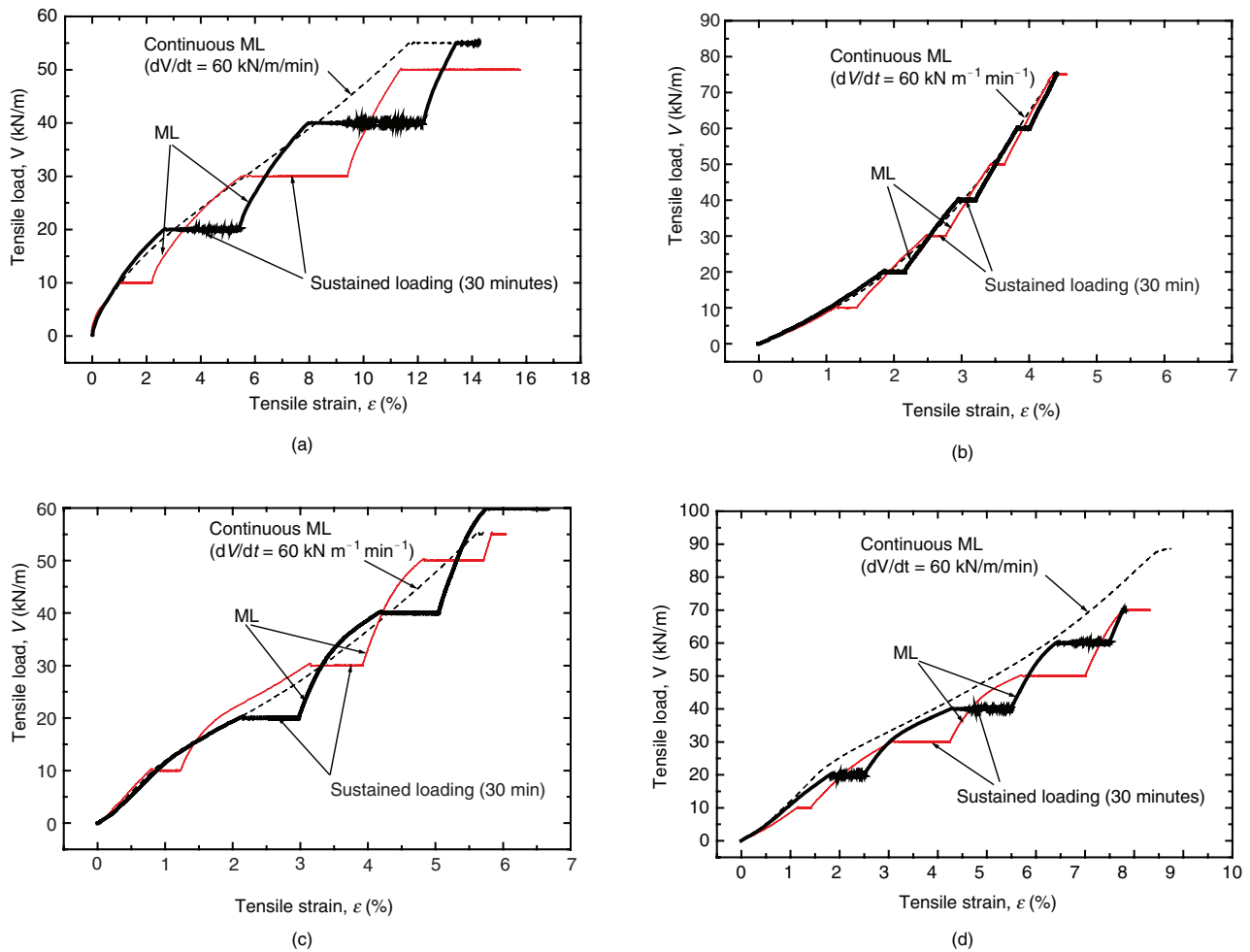


**Figure 23.** Tensile load–strain relationships from ML test at load rate  $dV/dt$  of  $60 \text{ kN m}^{-1} \text{ min}^{-1}$  with and without sustained loading stages for 30 min at each stage: (a) Geogrid A (HDPE); (b) Geogrid B (polyarylate); (c) Geogrid C (polyvinyl alcohol); (d) Geocomposite D (polyester yarns)

from Figures 24 and 25 that the developing rate of residual strain during the respective CL history lies in between those during the two sustained loading tests performed at the minimum load,  $V_0$ , and the maximum load,  $V_0 + \Delta V$ , of the respective CL history.

To compare the residual strain caused by a given cyclic loading history with that caused by the sustained loading histories applied at the minimum load,  $V_0$ , and the maximum load,  $V_0 + \Delta V$ , during the cyclic loading history under loading conditions that are otherwise the same, the residual strains are defined as follows, referring to Figure 26:

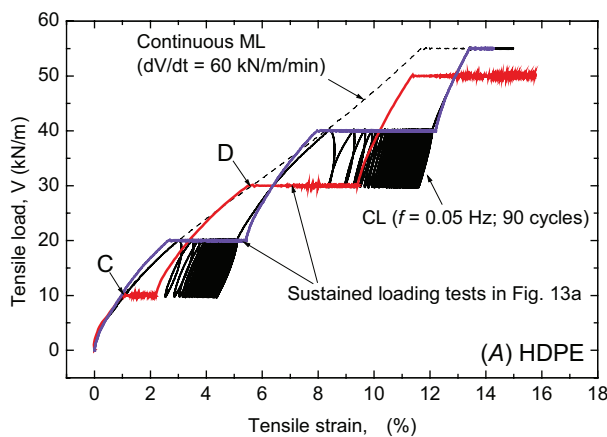
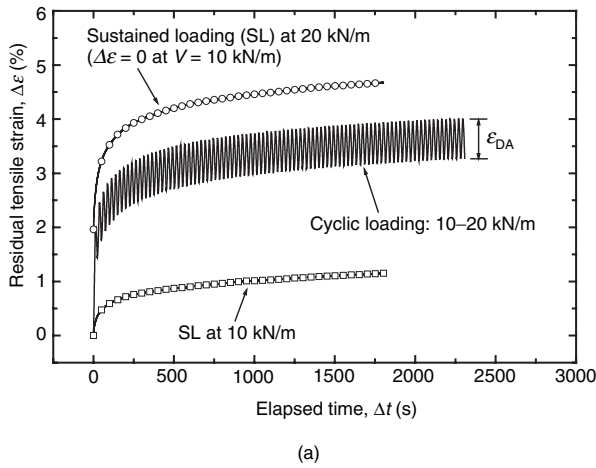
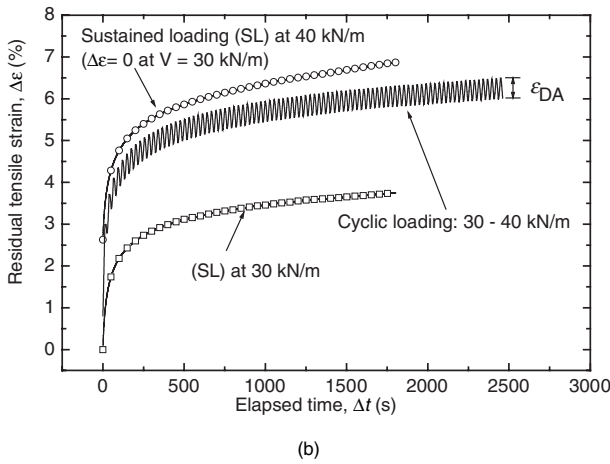


**Figure 24.** Tensile load–strain relationships for Geogrid A (HDPE) from ML tests with and without either sustained loading (SL) at several levels or cyclic loading (CL) at  $f = 0.05 \text{ Hz}$  (nominal value)

- Residual strain caused by cyclic loading,  $\Delta\epsilon_{CL}$ , is defined as the residual strain value when the load returns to the base load.
- Residual strain caused by sustained loading at the minimum load,  $V_0$ , is defined as  $\Delta\epsilon_{CP1}$ .
- Residual strain caused by sustained loading at the maximum load,  $V_0 + \Delta V$ , is defined as  $\Delta\epsilon_{ML} + \Delta\epsilon_{CP2} - \Delta\epsilon_{RE}$ , where  $\Delta\epsilon_{ML}$  is the strain increment that takes place by increasing the load from the base load,  $V_0$ , to the sustained load (equal to the maximum load,  $V_0 + \Delta V$ ),  $\Delta\epsilon_{CP2}$  is the creep strain increment that takes place during the sustained loading phase, and  $\Delta\epsilon_{RE}$  is the strain recovery that takes place by decreasing the load from the sustained load to the base load.



(a)



(b)

**Figure 25.** Time histories for Geogrid A (HDPE) of residual strain obtained from cyclic loading (CL) and sustained loading (SL) at both respective positive and negative peaks of cyclic loading amplitude as shown in Figure 24

Figure 27 summarises these comparisons, showing the relationships between the residual strains observed at an elapsed time of 1800 s in the respective cyclic loading performed at an amplitude equal to 10 kN/m and the

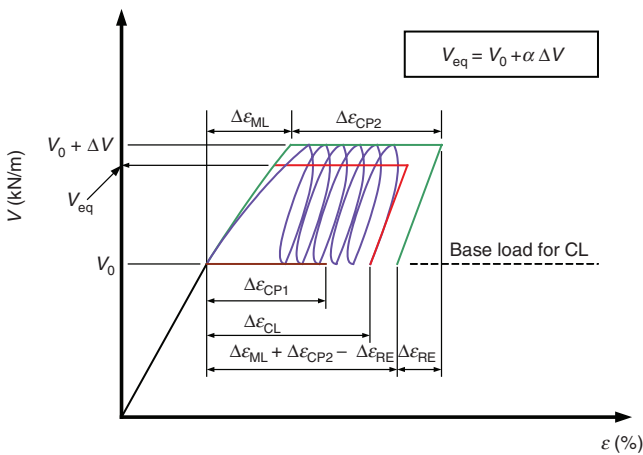


**Figure 26.** Definition of equivalent creep load for a given cyclic loading history

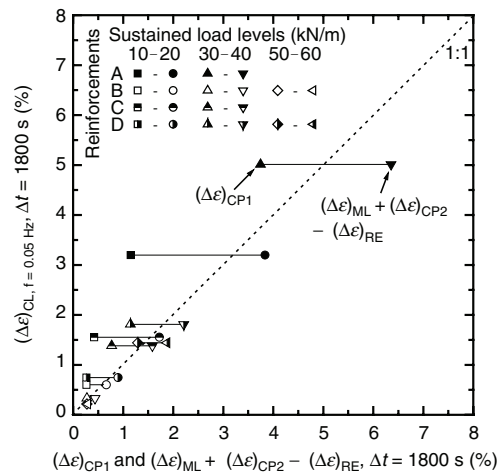


**Figure 27.** Comparison of cyclic residual strains with creep strains at an elapsed time of 1800 s

corresponding sustained loading tests performed at the minimum load,  $V_0$ , and the maximum load,  $V_0 + \Delta V$ , during the cyclic loading. The following trends in behaviour may be seen from Figures 24, 25 and 27:

- The manner of residual tensile strain development with time was very similar in the corresponding cyclic and sustained loading tests performed under otherwise the same conditions.
- The residual strain that developed during the respective CL history was in between the corresponding two sustained loading tests performed at the maximum and minimum tensile loads during the CL history.

To examine the second feature in more detail, the equivalent creep load,  $V_{eq}$ , was defined as the sustained load for which the residual strain,  $\Delta\epsilon_{ML} + \Delta\epsilon_{ep} - \Delta\epsilon_{RE}$ , becomes the same as the residual strain developed by a given cyclic loading history,  $\Delta\epsilon_{CL}$  (see Figure 26), where  $\Delta\epsilon_{CP}$  is the residual strain increment by sustained loading at  $V_{eq}$ . The parameter  $\alpha$  is then defined as follows:

$$V_{eq} = V_0 + \alpha\Delta V \tag{1}$$

The parameter  $\alpha$  indicates the magnitude of the equivalent creep load,  $V_{eq}$ , relative to the maximum and minimum loads of a given CL history, causing the same residual strain for the same loading period. Figure 28a shows the relationships between  $\alpha$  obtained for the different test conditions examined in the present study and the curvature of the segment of the load–strain relation,  $\partial^2 V / \partial \epsilon^2$  (kN/m), for the load range during the respective CL history. This plot was made by considering that the curvature might affect the value of  $\alpha$ . To this end, the two-degree polynomial function was fitted to the respective segment of the load–strain curve. It may be seen from Figure 28a that no systematic effects of reinforcement type, loading frequency or the curvature of the load–strain curve,  $\partial^2 V / \partial \epsilon^2$ , on the value of  $\alpha$  can be seen. Rather, the value of  $\alpha$  value tends to decrease with an increase in the base load level of CL. To

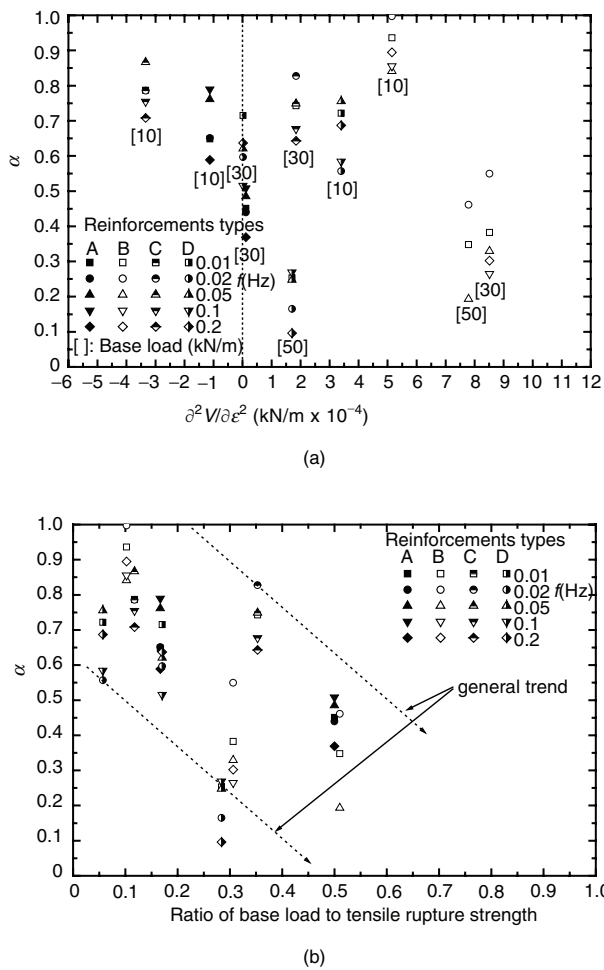


**Figure 28. Relationship between parameter  $\alpha$  and: (a)  $\partial^2 V / \partial \epsilon^2$ ; (b) normalised load level constructed based on the data presented in Figures 11 through 14**

examine this point, the relationships between  $\alpha$  and the ratio of the base load,  $V_0$ , to the tensile rupture strength were obtained, as shown in Figure 28b. It may be seen that  $\alpha$  tends to decrease as the tensile rupture condition is approached. The reason for this trend is not understood at present. It may be seen from Figures 28a and 28b that most of the values of  $\alpha$  are smaller than about 0.8. Based on this fact, it is recommended that  $\alpha = 0.8$  is taken as being conservatively safe for design when predicting the residual strain that would develop during a given cyclic loading history by performing an equivalent creep loading test.

The results presented above also indicate that the development of residual strain during a given CL history is not controlled by the rate-independent cyclic loading effects, but obviously it is controlled by the viscous properties as well as the increase in the irreversible strain by an increase in the load level associated with the application of cyclic load (Kongkitkul *et al.* 2004b). It is shown below that the entire tensile load and strain behaviour obtained from the tests performed in the present study can be simulated very well by a non-linear model that takes into account the viscous properties of the materials but not the rate-independent cyclic loading effects.

## 5. THREE-COMPONENT MODEL

### 5.1. Non-linear three-component model

Hirakawa *et al.* (2003) performed ML tests at different strain rates with and without step changes in the strain rate and sustained loading at intermediate stages on several types of geosynthetic reinforcement, including Geogrids A, B and C tested in the present study. They showed that all the relations obtained between tensile load, tensile strain and time can be simulated very well by a non-linear three-component model that was originally developed for geomaterials (i.e. soils and rocks) (Figure 29). The model is one of the sophisticated versions of the classical linear three-component model, which consists of a linear elastic component connected in series to another pair of linear elastic components connected in parallel to a Newtonian viscous component. The three components of the model (Figure 29) are all non-linear: that is, a hypoelastic component is connected in series to a pair of non-linear elastoplastic components connected in parallel to a non-linear viscous component. By introducing non-linearity into the three components, the model can realistically simulate the stress–strain–time behaviour both of geomaterials (Di Benedetto *et al.* 2002; Tatsuoka *et al.* 2002) and of polymer geosynthetic reinforcement (Hirakawa *et al.* 2003).

According to the non-linear three-component model (Figure 29), a given strain,  $\epsilon$ , consists of elastic and inelastic (or viscoplastic or irreversible) components,  $\epsilon^e$  and  $\epsilon^{ir}$ :

$$\epsilon = \epsilon^e + \epsilon^{ir} \tag{2}$$

The elastic strain is obtained as  $\epsilon^e = \int d\epsilon^e$ , where  $d\epsilon^e$  is the elastic strain increment. In the present study,  $d\epsilon^e$  was obtained as  $dV/E_{eq}(V)$ , where  $E_{eq}(V)$  is the elastic modulus, which is a function of the instantaneous tensile load. In so doing, the stress  $\sigma$  in the original model (Figure 29) was replaced by the tensile load per width of reinforcement,  $V$ . Then, the tensile load,  $V$ , for ML is obtained as

$$V = V^f(\epsilon^{ir}) + V^v \tag{3}$$

where  $V^f(\epsilon^{ir})$  is the inviscid load component, which is a unique function of  $\epsilon^{ir}$ . As Hirakawa *et al.* (2003) showed, for cyclic loading histories with a small load amplitude

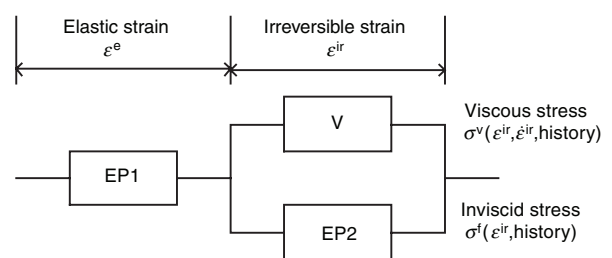


**Figure 29. Framework of the three-component model (Di Benedetto *et al.* 2002; Tatsuoka *et al.* 2002)**

the load–strain relation becomes essentially elastic, exhibiting the relation  $dV \approx E_{eq}(V) \cdot d\varepsilon$ .  $V^v$  is the viscous load component. Hirakawa *et al.* (2003) introduced the following two types of viscosity in their simulations:

- *Isotach viscosity*: For ML,  $V^v$  is always a unique function of instantaneous irreversible strain,  $\varepsilon^{ir}$ , and its rate,  $\dot{\varepsilon}^{ir}$  ( $= \dot{\varepsilon} - \dot{\varepsilon}^e$ , where  $\dot{\varepsilon}^e$  is the elastic strain rate).
- *Combined viscosity*:  $V^v$  consists of an isotach component and a so-called TESRA component, which decays with an increase in the irreversible strain (Di Benedetto *et al.* 2002; Tatsuoka *et al.* 2002).

In the present study, only the isotach type of viscosity is used, as this type has been known to be relevant to Geogrids A, B and C (Hirakawa *et al.* 2003) and also Geocomposite D, as shown later.

**5.2. Reference load–strain relation during monotonic loading**

With the isotach type of viscosity, the load–strain state ultimately reaches a rate-independent  $V^f-\varepsilon^{ir}$  relation (called the reference load–strain relation) during sustained loading at a constant load. In addition, the  $V-\varepsilon$  relation during continuous ML approaches the reference relation as the irreversible strain rate,  $\dot{\varepsilon}^{ir}$ , approaches zero. Referring to this theoretical framework, the reference relation in the case of monotonic loading for the respective type of geosynthetic reinforcement was inferred and fitted by the following polynomial equation:

$$V^f = f(\varepsilon^{ir}) = \sum_{i=1}^{10} a_i (\varepsilon^{ir})^{i-1} \tag{4}$$

where  $a_i$  is the coefficient for term  $i$ , which was determined so that Equation 4 could best fit the respective inferred  $V^f-\varepsilon^{ir}$  relation. The values of  $a_i$  were obtained separately for different specimens even for the same material, in view of the inevitable variability of material properties between different specimens. The values of  $a_i$  are listed, for the continuous ML tests only, in Table 3.

**5.3. Isotach-type viscous component for monotonic loading**

Hirakawa *et al.* (2003) showed that the jump in tensile load,  $\Delta V$ , observed upon a stepwise change in the tensile strain rate during otherwise monotonic loading is always proportional to the instantaneous tensile load,  $V$ , for all the types of geosynthetic reinforcement tested. This fact indicates that the isotach-type viscous tensile load,  $V_{iso}^v(\varepsilon^{ir}, \dot{\varepsilon}^{ir})$ , is always proportional to the instantaneous inviscid tensile load,  $V^f(\varepsilon^{ir})$ , as follows:

$$V_{iso}^v(\varepsilon^{ir}, \dot{\varepsilon}^{ir}) = V^f(\varepsilon^{ir}) g_v(\dot{\varepsilon}^{ir}) \tag{5}$$

where  $V_{iso}^v(\varepsilon^{ir}, \dot{\varepsilon}^{ir})$  is the isotach-type viscous load component that is a unique function of instantaneous values of  $\varepsilon^{ir}$  and  $\dot{\varepsilon}^{ir}$ , and  $g_v(\dot{\varepsilon}^{ir})$  is the viscosity function, which is always positive whether  $\dot{\varepsilon}^{ir}$  is positive or negative, and is given as follows (Di Benedetto *et al.* 2002; Tatsuoka *et al.* 2002):

$$g_v(\dot{\varepsilon}^{ir}) = \alpha \left\{ 1 - \exp \left[ 1 - \left( \frac{|\dot{\varepsilon}^{ir}|}{\dot{\varepsilon}_r^{ir}} + 1 \right)^m \right] \right\} (\geq 0) \tag{6}$$

where  $|\dot{\varepsilon}^{ir}|$  is the absolute value of  $\dot{\varepsilon}^{ir}$ , and  $\alpha$ ,  $m$  and  $\dot{\varepsilon}_r^{ir}$  are positive material constants. Hirakawa *et al.* (2003) determined these parameters experimentally for Geogrids A, B and C, and Kongkitkul *et al.* (2004a) determined them for Geocomposite D (see Table 3).

**5.4. Reference load–strain relation during cyclic loading**

To simulate the  $V-\varepsilon$  relations during a given cyclic loading history, Equation 3 should be revised as follows:

$$V = V^f(\varepsilon^{ir}, h_s) + V_{iso}^v(\varepsilon^{ir}, \dot{\varepsilon}^{ir}, h_s) \tag{7}$$

where  $h_s$  is the parameter representing the loading history. The relationship between the tensile load,  $V^f(\varepsilon^{ir}, h_s)$ , and the irreversible tensile strain,  $\varepsilon^{ir}$ , during a given cyclic loading history was obtained as follows by referring to the proportional rule that was developed for sand (Tatsuoka *et al.* 2003). The following two cases were introduced to alleviate the problem that the shapes of the load–strain relation during primary tensile loading

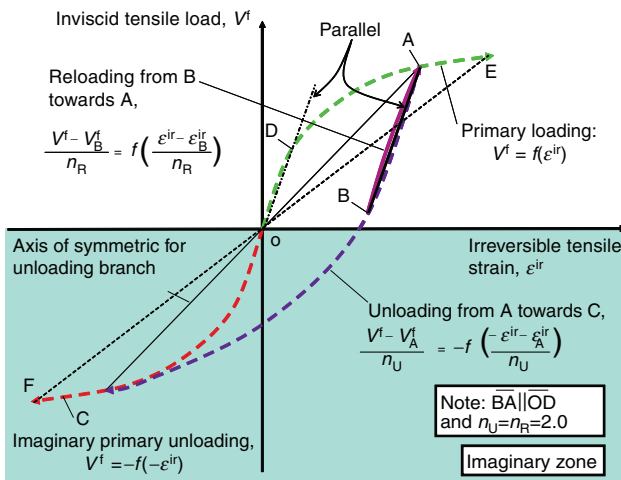
**Table 3. Parameters of the viscosity function used in the model simulation**

		Reinforcement types			
		A	B	C	D
Viscous parameters	$\alpha$	1.6	0.44	0.76	0.52
	$m$ ( $d\varepsilon^{ir}/dt$ ) <sub>r</sub> (%/s)	0.085	0.09	0.12	0.08
		0.00035	0.0001	0.0001	0.0001
Coefficients $a_i$ in Equation 4 for ML tests	$i = 0$	0	0	0	0
	$i = 1$	10.94115	7.6578	26.458	17.303
	$i = 2$	−4.50274	−8.3573	−31.023	−0.5734
	$i = 3$	1.34908	26.141	21.775	−2.1565
	$i = 4$	−0.23528	−25.018	−7.4159	0.8087
	$i = 5$	0.02468	10.287	1.2421	−0.108
	$i = 6$	−0.00153	−1.3897	−0.0806	0.0052
	$i = 7$	$5.16 \times 10^{-5}$	0	0	0
	$i = 8$	$−7.26 \times 10^{-7}$	0	0	0
	$i = 9$	0	0	0	0

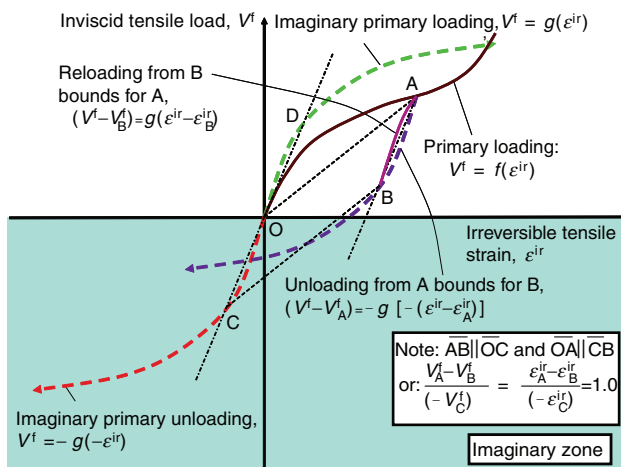
and cyclic loading are either similar (as with drained sands and clays), or completely different depending on the type of geosynthetic reinforcement. It was assumed that the load–strain curves during unloading and subsequent reloading are symmetric in both cases.

5.4.1. Case 1

This case is suitable for Geogrid A, which does not exhibit a strong trend of S-shaped load–strain curve during primary loading (see Figure 4). In this case, the unloading and reloading curves can be obtained by properly scaling and shifting the primary tensile loading curve,  $V^f = f(\epsilon^{ir})$ , as illustrated in Figure 30a. The imaginary primary unloading curve, for which the load is in compression, was introduced to derive the unloading and reloading curves. Note that any part of the load–strain curve where the load is negative (i.e. in compression) illustrated in Figure 30a is imaginary. According to the assumption described above, the primary unloading curve was represented by  $V^f = -f(-\epsilon^{ir})$ .



(a)



(b)

Figure 30. Proportional rule using: (a) the same function for loading, unloading, and reloading; (b) implementation of different function for unloading and reloading to simulate tensile load–strain relationship during cyclic loading

Herein, ‘loading’ and ‘unloading’ are referred to cases where the irreversible tensile strain increment,  $d\epsilon^{ir}$ , is, respectively, positive (tensile) and negative (compressive).

According to the proportional rule (Tatsuoka *et al.* 2003), upon reversal of the loading direction, either the external or the internal rule is chosen for a given loading history, based on the magnitude of the current irreversible tensile strain,  $\epsilon^{ir}$ , relative to the instantaneous maximum and minimum reference tensile strains,  $\epsilon_{max}^{ir}$  and  $\epsilon_{min}^{ir}$ , the meaning of which is explained below. To maintain continuity between the external and internal rules, it was assumed that a pair of points having the coordinates of  $\epsilon_{max}^{ir}$  and  $\epsilon_{min}^{ir}$  are always located on the opposite sides of the origin (point O) on a straight line passing through the origin, such as A–O–C (Figure 30a).

1. Suppose that loading (with positive  $d\epsilon^{ir}$ ) starts from the origin (point O) and continues until point A following the primary loading relation,  $V^f = f(\epsilon^{ir})$ . Then we define  $\epsilon_{max}^{ir}$  at point A, which is the maximum value of  $\epsilon^{ir}$  ever achieved by loading, as  $\epsilon_A^{ir}$ . Accordingly,  $\epsilon_{min}^{ir}$  at point B (located along the first unloading curve from point A) =  $\epsilon_A^{ir}$ . If the current  $\epsilon^{ir}$  value becomes larger than the previous value of  $\epsilon_{max}^{ir}$  (i.e. when  $\epsilon^{ir} > \epsilon_{max}^{ir} = \epsilon_A^{ir}$ ), the previous value of  $\epsilon_{max}^{ir}$  is replaced by the instantaneous  $\epsilon^{ir}$  value. For example, if loading continues from point A to point E, we obtain  $\epsilon_{max}^{ir} = \epsilon^{ir}$  at point E,  $\epsilon_E^{ir}$ .
2. The  $\epsilon_{min}^{ir}$  value is defined as the smaller value of (i) the smallest value of  $\epsilon^{ir}$  ever attained during unloading (with negative  $d\epsilon^{ir}$ ), and (ii) the  $\epsilon^{ir}$  value at the intersection of the straight line starting from the point of  $\epsilon_{max}^{ir}$  and passing the origin O with the primary unloading curve,  $V^f = -f(-\epsilon^{ir})$ . In Figure 30a we obtain  $\epsilon_{min}^{ir}$  at point B =  $\epsilon_C^{ir}$  at point A, corresponding to point A.
3. The  $\epsilon_{max}^{ir}$  value is then defined as the larger value of (i) the largest value of  $\epsilon^{ir}$  ever attained by loading (with positive  $d\epsilon^{ir}$ ), and (ii) the  $\epsilon^{ir}$  value at the intersection of the straight line starting from the point of  $\epsilon_{min}^{ir}$  and passing through the origin O with the primary loading curve,  $V^f = f(\epsilon^{ir})$ . For example, we obtain  $\epsilon_{max}^{ir}$  at point F =  $\epsilon_E^{ir}$  at point E, which is the intersection of the straight line starting from point F and passing through the origin O with the primary loading curve,  $V^f = f(\epsilon^{ir})$ .

The hysteretic load–strain relations for cyclic loading illustrated in Figure 30a are obtained as follows:

1. During the first primary loading from origin O ( $\epsilon_O^{ir} = 0, V_O^f = 0$ ), where  $\epsilon_{max}^{ir} = \epsilon_{min}^{ir} = 0$ , until point A, we always have  $\epsilon_{max}^{ir} = \epsilon^{ir}$ , while the stress–strain curve follows the loading skeleton curve  $V^f = f(\epsilon^{ir})$ . At point A ( $\epsilon_A^{ir}, V_A^f$ ), we have  $\epsilon_{max}^{ir} = \epsilon_A^{ir}$  and  $\epsilon_{min}^{ir} = \epsilon_C^{ir}$ .
2. Suppose that loading is reversed at point A. The unloading curve, bound for point C, is obtained by following the external rule (with  $\epsilon_{max}^{ir} = \epsilon_A^{ir}$ ) and by using the known primary unloading curve,

$V^f = -f(-\epsilon^{ir})$ , and the coordinate at point C ( $\epsilon_C^{ir}, V_C^f$ ) as:

$$\frac{V^f - V_A^f}{n_U} = -f\left(-\frac{\epsilon^{ir} - \epsilon_A^{ir}}{n_U}\right); \text{ or}$$

$$V^f = V_A^f - n_U f\left(-\frac{\epsilon^{ir} - \epsilon_A^{ir}}{n_U}\right) \tag{8a}$$

$$n_U = \frac{(-V_C^f) + V_A^f}{V_A^f} = \frac{(-\epsilon_C^{ir}) + \epsilon_A^{ir}}{\epsilon_A^{ir}} (\geq 0) \tag{8b}$$

where  $n_U$  is assumed equal to 2.0 in the present study.

3. With geosynthetic reinforcement, reloading from a point on the primary unloading curve  $V^f = -f(-\epsilon^{ir})$ , along which the load  $V$  is negative (i.e. compressive), is not possible, but any reloading curve should start from a point on the unloading curve where the load is positive (tensile). When unloading is reversed to reloading at point B, where  $\epsilon^{ir}$  is in between  $\epsilon_{min}^{ir} = \epsilon_C^{ir}$  and  $\epsilon_{max}^{ir} = \epsilon_A^{ir}$  maintaining the previous values of  $\epsilon_{max}^{ir}$  and  $\epsilon_{min}^{ir}$ , the reloading curve (with positive  $d\epsilon^{ir}$ ) is assumed to be bound for the latest previous reversing point before point B (i.e. point A). The reloading curve is obtained by following the internal rule while scaling up the primary loading curve,  $V^f = f(\epsilon^{ir})$ , as:

$$\frac{V^f - V_B^f}{n_R} = f\left(\frac{\epsilon^{ir} - \epsilon_B^{ir}}{n_R}\right); \text{ or}$$

$$V^f = V_B^f + n_R f\left(\frac{\epsilon^{ir} - \epsilon_B^{ir}}{n_R}\right) \tag{9a}$$

$$n_R = \frac{V_A^f - V_B^f}{V_D^f} = \frac{\epsilon_A^{ir} - \epsilon_B^{ir}}{\epsilon_D^{ir}} (\geq 0) \tag{9b}$$

where point D ( $\epsilon_D^{ir}, V_D^f$ ) is the intersection of the straight line starting from the origin O while parallel to the straight line between points B and A with the primary loading curve. The parameter  $n_R$  must be equal to  $n_U$ , which is equal to 2.0 in the present case, in order to rejoin the primary loading curve at point A. However, the reloading curve does not rejoin the primary loading curve smoothly.

4. Suppose that the loading direction is reversed at point G between points B and A while  $\epsilon_{max}^{ir} \geq \epsilon^{ir} \geq \epsilon_{min}^{ir}$  maintaining the previous values of  $\epsilon_{max}^{ir}$  and  $\epsilon_{min}^{ir}$ . The re-unloading curve is assumed to be bound for the latest previous reversing point (i.e. point B), and is obtained by following the internal rule as

$$\frac{V^f - V_G^f}{n_3} = -f\left(-\frac{\epsilon^{ir} - \epsilon_G^{ir}}{n_3}\right); \text{ or}$$

$$V^f = V_G^f - n_3 f\left(-\frac{\epsilon^{ir} - \epsilon_G^{ir}}{n_3}\right) \tag{10a}$$

$$n_3 = \frac{V_G^f - V_B^f}{V_J^f} = \frac{\epsilon_G^{ir} - \epsilon_B^{ir}}{\epsilon_J^{ir}} (\geq 0) \tag{10b}$$

where point J ( $\epsilon_J^{ir}, V_J^f$ ) is the intersection of the straight line starting from the origin O while parallel to the straight line between points G and B with the primary loading curve  $V^f = f(\epsilon^{ir})$ . Again, the parameter  $n_3$  must be equal to  $n_U$ , which is equal to 2.0 in the present case, in order to rejoin the previous unloading curve at point B. At point B, the re-unloading curve does not rejoin the previous unloading curve  $A \rightarrow B \rightarrow C$  smoothly.

5. Whenever the previous reversing point is passed (for example when point B is passed after following re-unloading branch  $G \rightarrow B$ ), all memory of the previous cyclic loading history is erased.

#### 5.4.2. Case 2

Some types of geosynthetic reinforcement have a noticeably S-shaped primary load-strain curve, and the shape of the load-strain curves during unloading/reloading is largely different from that of the primary loading curve. This is the case with Geogrids B and C and Geocomposite D (see Figures 5, 6 and 7). In this case it becomes necessary to introduce imaginary primary loading and unloading curves,  $V^f = g(\epsilon^{ir})$  and  $V^f = -g(-\epsilon^{ir})$ , which have a shape that is similar to the shape of actual unloading and reloading curves, but different from the actual primary loading curve,  $V^f = f(\epsilon^{ir})$ , as illustrated in Figure 30b. Hysteretic curves during cyclic loading are obtained by shifting these imaginary primary loading and unloading curves (without scaling). A polynomial function was determined for  $V^f = g(\epsilon^{ir})$  so that it could be best fit to the inferred curves of inviscid tensile load against irreversible strain (at zero irreversible strain rate) during unloading and reloading. The hysteretic load-strain relations during cyclic loading illustrated in Figure 30b are obtained as follows:

1. During the first primary loading from the origin O ( $\epsilon_O^{ir} = 0, V_O^f = 0$ ) until point A, the load-strain curve follows the primary loading curve,  $V^f = f(\epsilon^{ir})$ .
2. Suppose that loading is reversed at point A. The unloading curve is obtained by using the known imaginary primary unloading curve  $V^f = -g(-\epsilon^{ir})$  and the coordinate at point A ( $\epsilon_A^{ir}, V_A^f$ ) as:

$$(V^f - V_A^f) = -g[-(\epsilon^{ir} - \epsilon_A^{ir})] \tag{11a}$$

$$\frac{V_A^f - V_B^f}{-(V_C^f)} = \frac{\epsilon_A^{ir} - \epsilon_B^{ir}}{-(\epsilon_C^{ir})} = 1.0 \tag{11b}$$

where point C ( $\epsilon_C^{ir}, V_C^f$ ) is the intersection of the straight line starting from the origin O while parallel to the straight line between points A and B with the imaginary primary unloading curve  $V^f = -g(-\epsilon^{ir})$ .

3. When unloading is reversed to reloading at point B, the reloading curve (with positive  $d\epsilon^{ir}$ ), bound for the latest previous reversing point before point B (i.e.

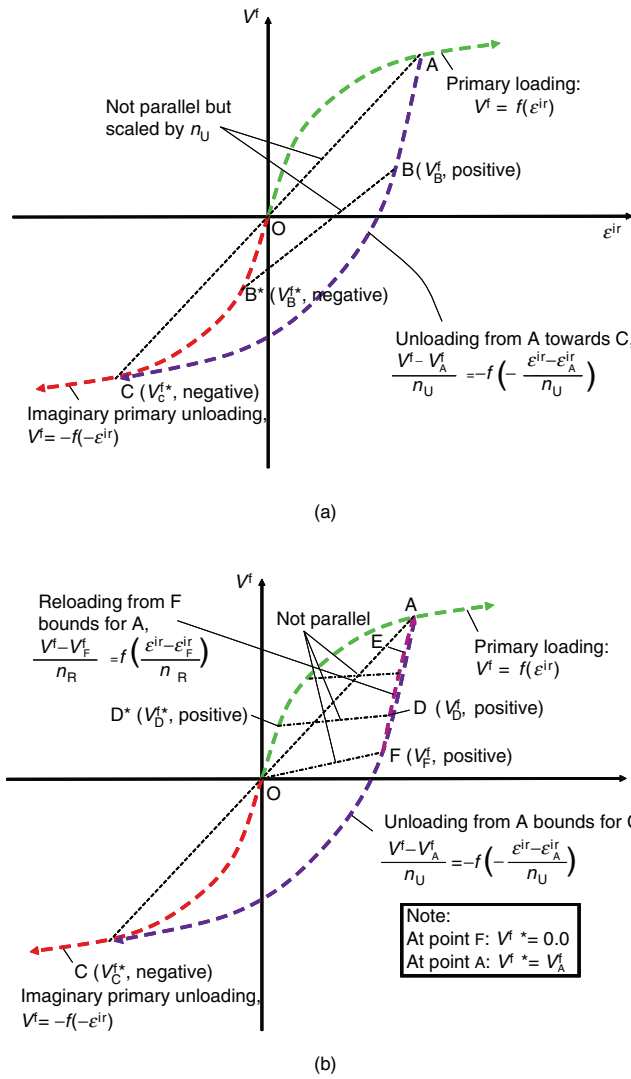


Figure 31. Proportional rule to obtain the viscous load component (in case of Figure 30a) during: (a) unloading; (b) reloading

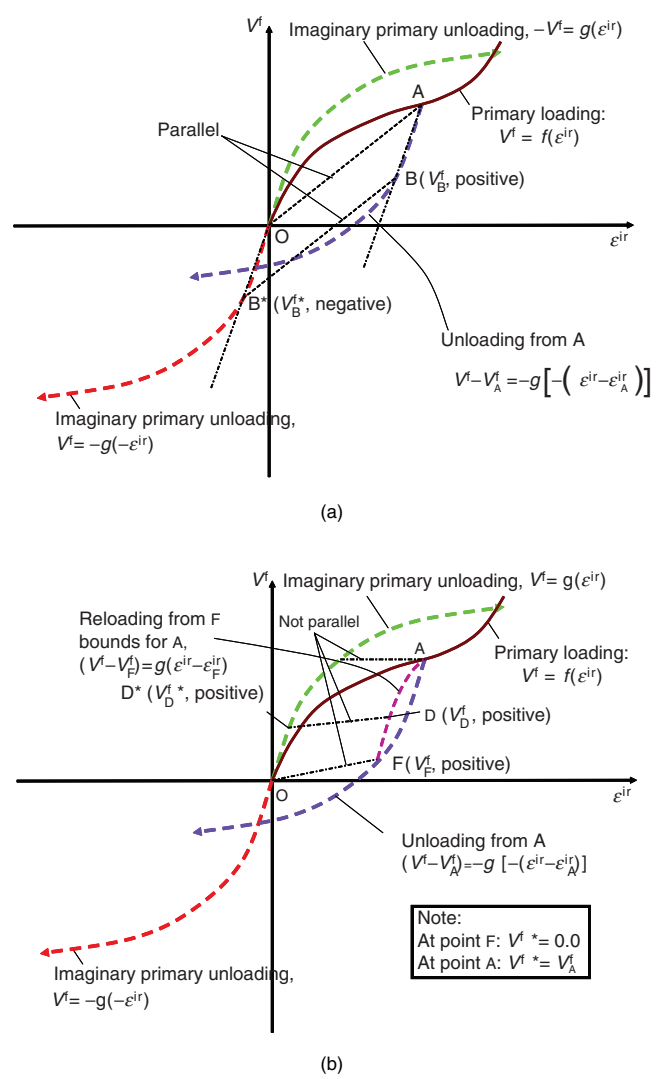


Figure 32. Method to obtain the viscous load component (in case of Figure 30b) during: (a) unloading (without scaling); (b) reloading (with scaling to join smoothly at point A)

point A), is obtained by shifting the imaginary primary loading curve as

$$(V^f - V_B^f) = g(\epsilon^{ir} - \epsilon_B^{ir}) \tag{12a}$$

$$\frac{V_A^f - V_B^f}{V_D^f} = \frac{\epsilon_A^{ir} - \epsilon_B^{ir}}{\epsilon_D^{ir}} = 1.0 \tag{12b}$$

where point D ( $\epsilon_D^{ir}, V_D^f$ ) is the intersection of the straight line starting from the origin O while parallel to the straight line between points B and A with the imaginary primary loading curve  $V^f = g(\epsilon^{ir})$ . The reloading curve rejoins the primary loading curve,  $V^f = f(\epsilon^{ir})$ , at point A, but not smoothly.

- The behaviour during re-unloading can be obtained as in Case 1.

### 5.5. Isotach-type viscous load component during cyclic loading

The isotach type of viscous load component,  $V_{iso}^v(\epsilon^{ir}, \dot{\epsilon}^{ir}, h_s)$ , is positive during primary loading,

reloading, re-reloading, re-unloading and so on (when  $d\epsilon^{ir}$  is positive), and it is negative during unloading and so on (when  $d\epsilon^{ir}$  is negative). It is natural to assume that the viscous load component,  $V^v$ , is zero at the start of unloading, reloading and so on. For these reasons, it was assumed that the value of  $V_{iso}^v(\epsilon^{ir}, \dot{\epsilon}^{ir}, h_s)$  for both unloading and reloading conditions is given as

$$V_{iso}^v(\epsilon^{ir}, \dot{\epsilon}^{ir}, h_s) = V^{f*} g_v(\dot{\epsilon}^{ir}) \tag{13}$$

where  $V^{f*}$  is the inviscid load component used only to obtain the viscous load component, and is obtained as follows.

#### 5.5.1. For $V^f - \dot{\epsilon}^{ir}$ relations in Case 1 (Geogrid A)

For the value of  $V_{iso}^v(\epsilon^{ir}, \dot{\epsilon}^{ir}, h_s)$  at point B during unloading (Figure 31a),  $V^{f*}$  is the value of  $V^f$  at point B\* along the imaginary primary unloading curve that corresponds to point B, obtained as

$$V^{f*} = \frac{V_B^f - V_A^f}{n_U} (\leq 0) \tag{14}$$

where  $n_U = 2.0$  (in the present case). In this case,  $V^{f*}$  is negative.

For the value of  $V_{iso}^v(\epsilon^{ir}, \dot{\epsilon}^{ir}, h_s)$  at point D during reloading (Figure 31b),  $V^{f*}$  is the value of  $V^f$  at point D\* along the primary loading curve that corresponds to point D, obtained as

$$V^{f*} = \frac{V_D^f - V_F^f}{V_A^f - V_F^f} V_A^f \quad (\geq 0) \tag{15}$$

5.5.2. For  $V^f - \epsilon^{ir}$  relations in Case 2 (Geogrids B and C and Geocomposite D)

For the value of  $V_{iso}^v(\epsilon^{ir}, \dot{\epsilon}^{ir}, h_s)$  at point B during unloading (Figure 32a),  $V^{f*}$  is the value of  $V^f$  at point B\* along the imaginary primary unloading curve that corresponds to point B, obtained as

$$V^{f*} = V_B^f - V_A^f \quad (\leq 0) \tag{16}$$

In this case,  $V^{f*}$  is negative.

For the value of  $V_{iso}^v(\epsilon^{ir}, \dot{\epsilon}^{ir}, h_s)$  at point D during reloading (Figure 32b),  $V^{f*}$  is the value of  $V^f$  at point D\*

along the imaginary primary loading curve that corresponds to point D, obtained as

$$V^{f*} = \frac{V_D^f - V_F^f}{V_A^f - V_F^f} V_A^f \quad (\geq 0) \tag{17}$$

The value of  $V^{f*}$  when the respective reloading curve rejoins the actual primary loading curve  $V^f = f(\epsilon^{ir})$  at point A that is obtained by following Equations 15 and 17 becomes  $V_A^f$  (i.e. the value before the unloading starts). Therefore the viscous load becomes continuous when the  $V^f - \epsilon^{ir}$  relation is shifted from a reloading curve towards the primary loading curve at point A without exhibiting any sudden change.

6. SIMULATIONS

6.1. Sustained loading tests

In the present study, it was first confirmed that the non-linear three-component model is able to simulate the results from load-controlled ML tests with and without sustained loading at multiple intermediate stages.

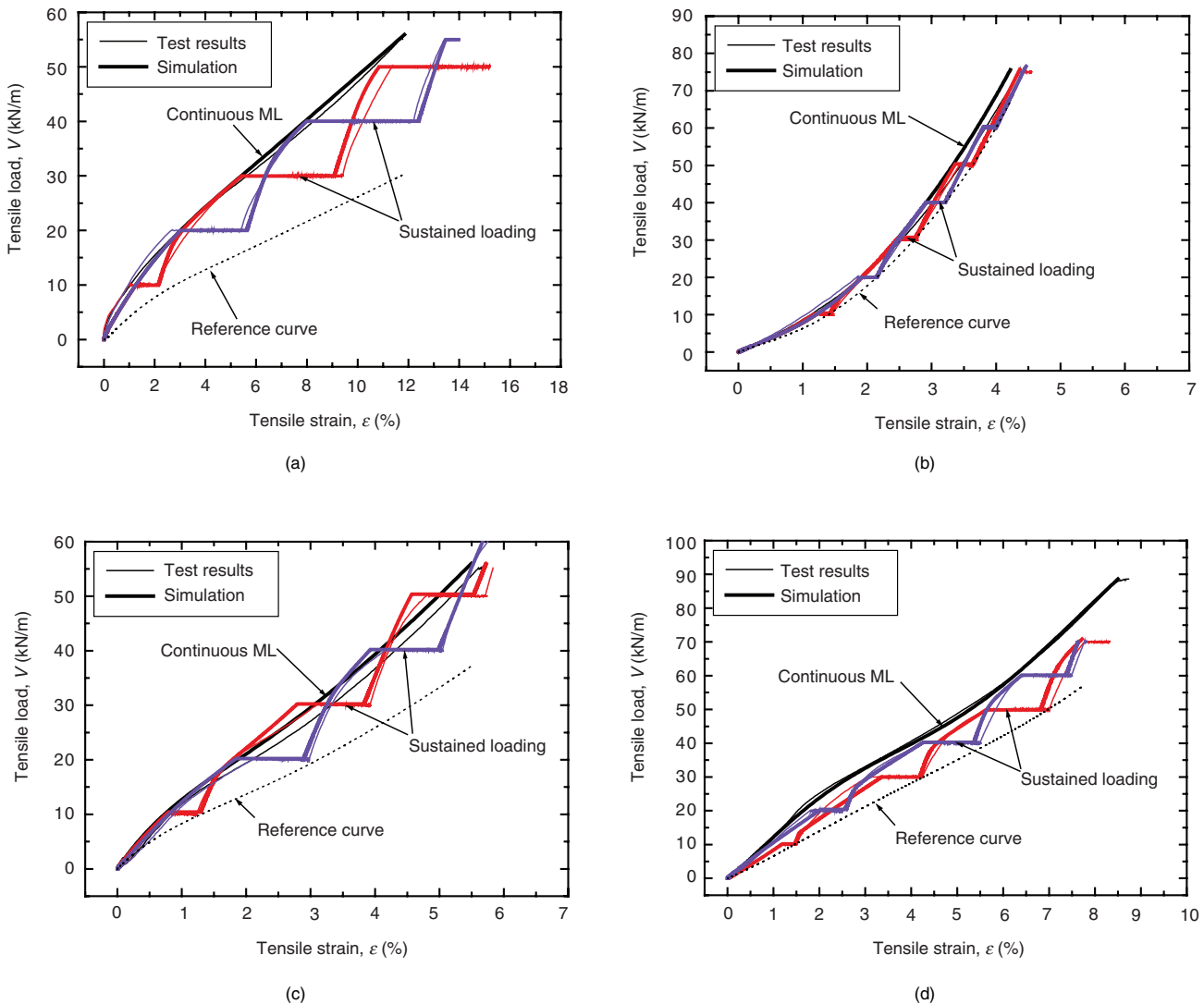


Figure 33. Simulation of sustained loading tests presented in Figure 23: (a) Geogrid A (HDPE); (b) Geogrid B (polyarylate); (c) Geogrid C (polyvinyl alcohol); (d) Geocomposite D (polyester yarns)

Figures 33a to 33d compare the results from such tests for the four types of geosynthetic reinforcement, presented in Figures 23a to 23d, and their simulations. The parameters of the viscosity function,  $g_v(\dot{\epsilon}^{ir})$ , that were used in the simulations are listed in Table 3. The parameters for Geogrids A, B and C are the same as those used by Hirakawa *et al.* (2003). The parameters for Geocomposite D were determined by performing another series of displacement-controlled tensile tests including stepwise changes in the strain rate, similar to the one performed by Hirakawa *et al.* (2003). Figure 34 compares the measured creep residual strains at an elapsed time equal to 1000 s with those from the model simulations for all the sustained loading tests performed in the present study. It may be seen from Figures 33 and 34 that the model is able to simulate very well the load–strain relations from the load-controlled tests with and without multiple-stages of sustained loading, and the amount of creep strain.

To validate whether the model is also able to simulate the viscous effects during monotonic unloading and reloading, the results from the two displacement-controlled tensile tests performed at an axial strain rate equal to  $\pm 1.0\%/min$  using Geogrids B and C reported by Hirakawa *et al.* (2003) were simulated (Figures 35a and 35b). In these tests, sustained loading tests were performed not only during primary loading but also during global unloading and reloading. The following trends in behaviour can be seen for both types of reinforcement:

- The creep strain during sustained loading under otherwise monotonic unloading becomes negative, and the amount of negative creep strain increases, with a decrease in the tensile load level.
- The creep strain during global reloading becomes positive again, but it is much smaller than that observed at the same sustained load level during primary loading.

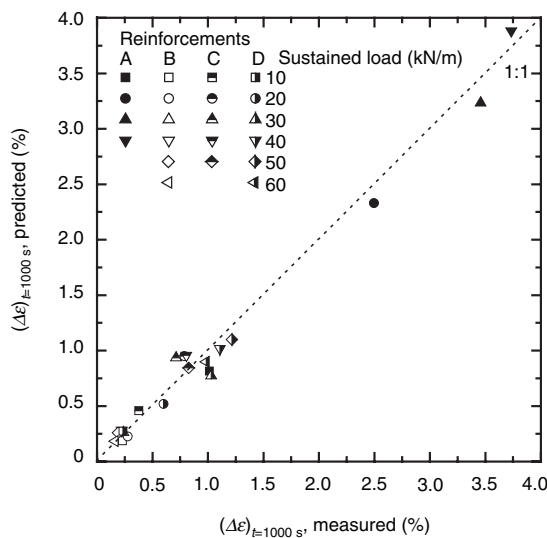
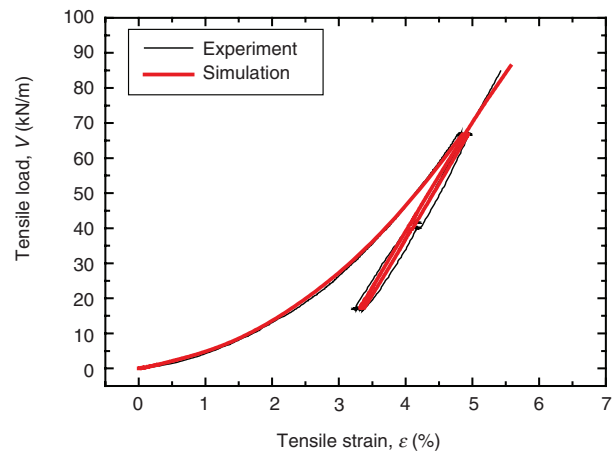
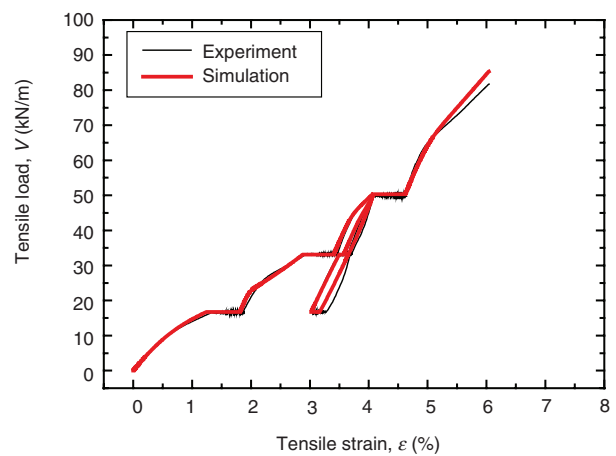


Figure 34. Comparison of predicted and measured creep residual strains at elapsed time of 1000 s



(a)



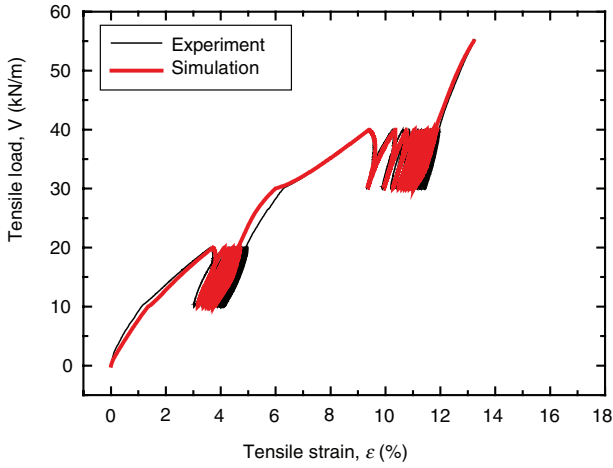
(b)

Figure 35. Simulation of tensile load–strain relationship from displacement-controlled tests including global unloading and reloading together with intermissions of sustained loading during unloading and reloading: (a) Geogrid B (polyarylate); (b) Geogrid C (polyvinyl alcohol)

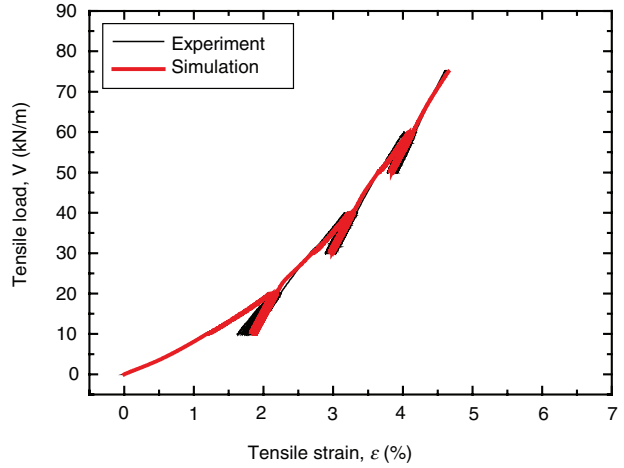
The results from simulations using the same model parameters as those used by Hirakawa *et al.* (2003) are also presented in these figures. It may be seen from Figure 35 that the model can simulate very well the time-dependent load–strain relations during global unloading and reloading. It is important to note that negative creep deformation taking place under unloaded conditions is properly simulated.

6.2. Cyclic loading tests

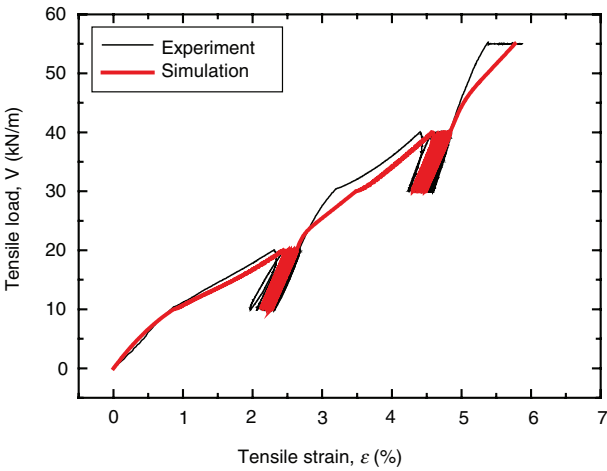
Figures 36a to 36d compare the results from the load-controlled ML tests including two or three cyclic loading stages at  $f = 0.01$  Hz with a load amplitude of 10 kN/m, presented in Figures 4a, 5a, 6a and 7a, and their simulations. Figures 37a and 37b compare the similar results for  $f = 0.01$  Hz and a load amplitude of 20 kN/m, presented in Figures 8a and 9a, and their simulations. The parameters of the viscosity function for Geogrids A through C in these simulations are the same as those



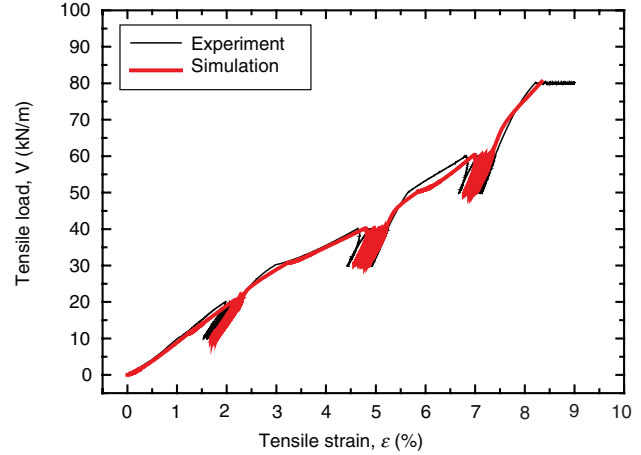
(a)



(b)

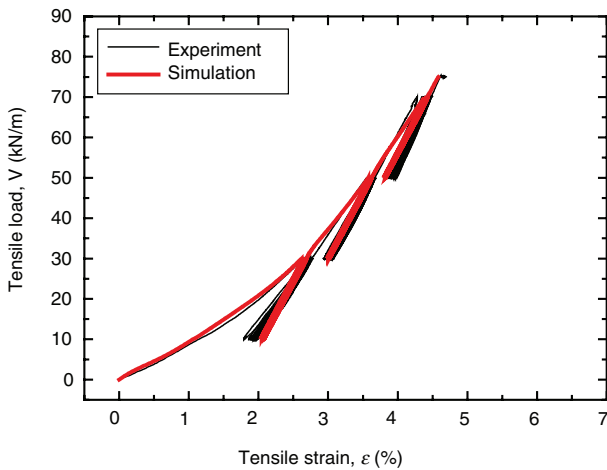


(c)

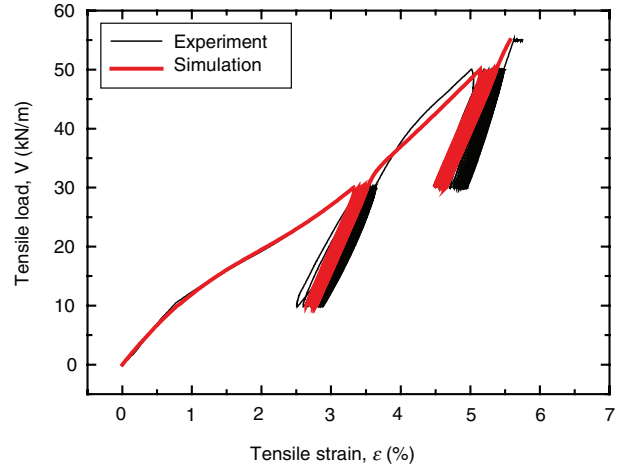


(d)

Figure 36. Simulation of cyclic loading tests presented in Figures 4a, 5a, 6a and 7a: (a) Geogrid A (HDPE); (b) Geogrid B (polyarylate); (c) Geogrid C (polyvinyl alcohol); (d) Geocomposite D (polyester yarns)

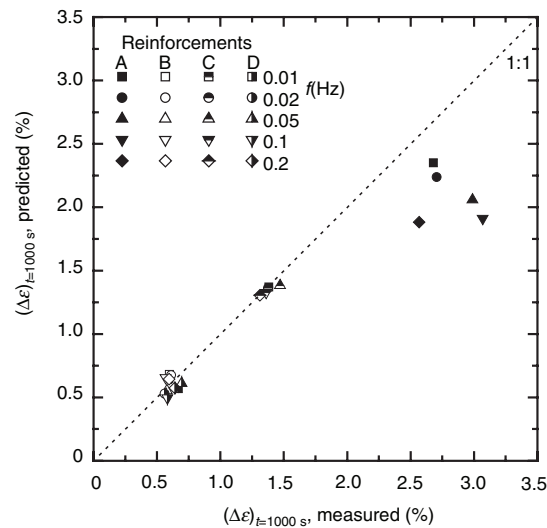


(a)

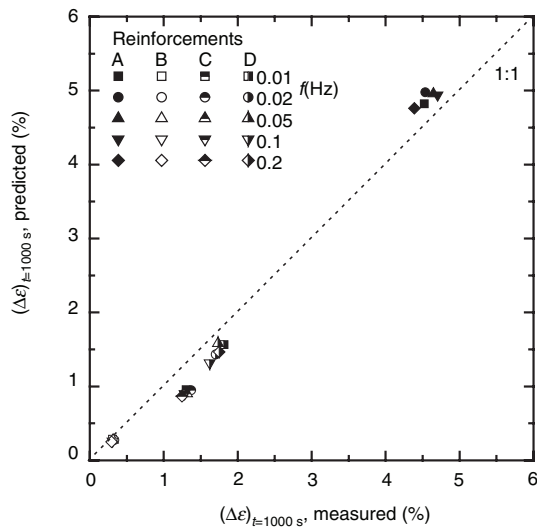


(b)

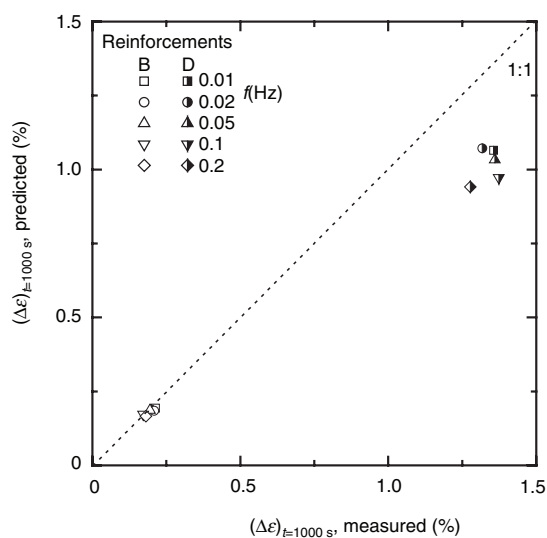
Figure 37. Simulation of cyclic loading tests presented in Figures 8a and 9a: (a) Geogrid B (polyarylate); (b) Geogrid C (polyvinyl alcohol)



(a)



(b)



(c)

**Figure 38. Comparison of predicted and measured cyclic residual strains at elapsed time of 1000 s obtained from cyclic loading tests with 10 kN/m amplitude: (a)  $V = 10\text{--}20$  kN/m; (b)  $V = 30\text{--}40$  kN/m; (c)  $V = 50\text{--}60$  kN/m**

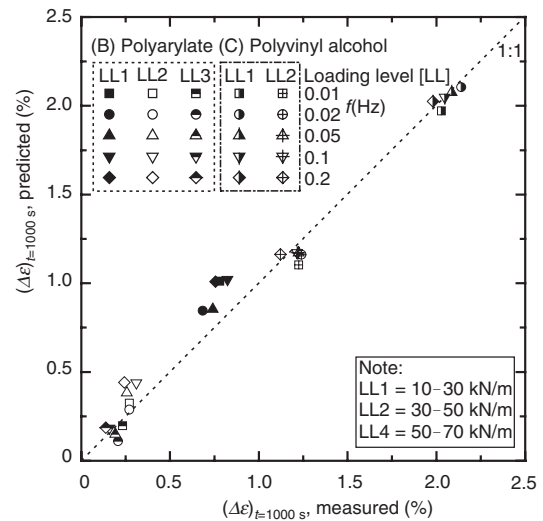


**Figure 39. Comparison of predicted and measured cyclic residual strains at elapsed time of 1000 s obtained from cyclic loading tests with 20 kN/m amplitude**

used by Hirakawa *et al.* (2003) (Table 3). Figures 38a, 38b and 38c compare the measured residual strains from all the cyclic loading tests with a load amplitude of 10 kN/m, lasting for a period of 1000 s (as presented in Figures 4 to 7), with their simulations. A similar comparison for a load amplitude of 20 kN/m, as shown in Figures 8 and 9, is presented in Figure 39. It may be seen from these figures that the proposed model can simulate rather accurately the whole viscous effects on the load–strain behaviour observed not only during monotonic loading but also at sustained and cyclic loading stages for all the tested types of geosynthetic reinforcement. It should be noted that any effects from rate-independent effects of cyclic loading were *not* taken into account in these model simulations. It should also be noted that the same parameters with respect to the viscous properties were used to simulate results of the same type of geosynthetic reinforcement from tests using different loading histories (i.e. displacement-controlled versus load-controlled, monotonic versus cyclic and sustained versus cyclic).

### 6.3. Sustained and cyclic loading tests

Finally, the test results presented in Figures 20a and 21a were simulated as shown in Figure 40. In these tests, a cyclic loading history was applied after a sustained loading history. It may be seen from this figure that the model can simulate very well the viscous effects seen during such consecutive sustained and cyclic loading histories following monotonic loading. This fact indicates again that the development of residual strain during a given cyclic loading history is due essentially to the viscous properties of polymer geosynthetic reinforcement in addition to the development of irreversible strain increments by an increase in the inviscid load associated with cyclic loading.

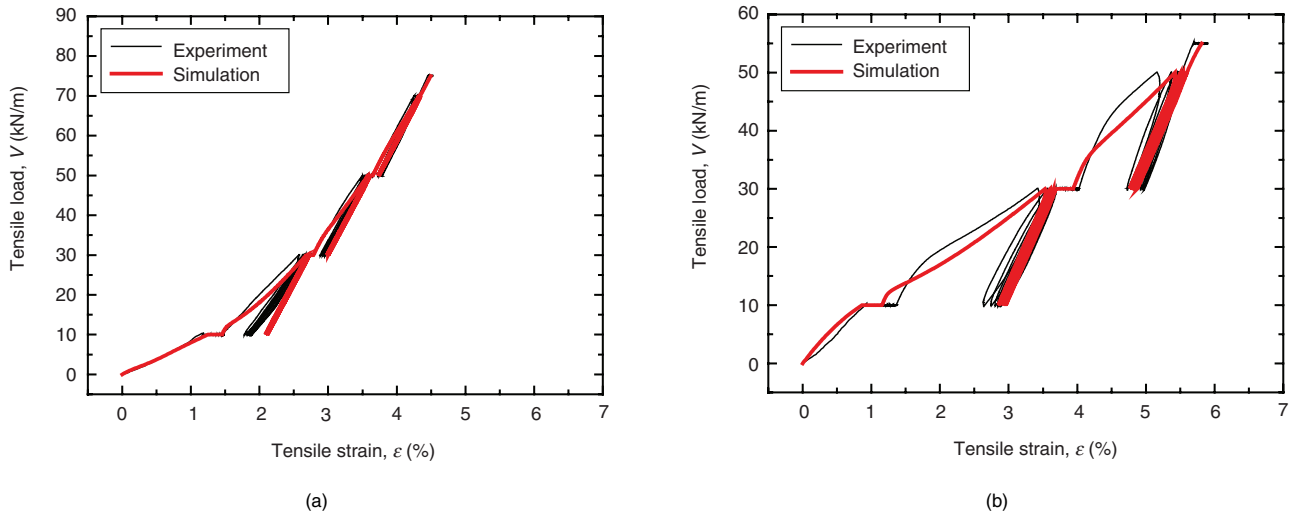


Figure 40. Simulation of cyclic loading with initial sustained loading tests presented in Figures 20a and 21a: (a) Geogrid B (polyarylate); (b) Geogrid C (polyvinyl alcohol)

## 7. CONCLUSIONS

The following conclusions can be derived from the results of experiments and simulations presented in this paper:

- Upon the restart of monotonic loading at a constant rate of strain or load after a sustained or cyclic loading history, the load–strain relation first exhibited a very high tangent stiffness for some load range and then tended to rejoin the original response curve that would have been obtained by continuous monotonic loading. Consequently, the effects of previous sustained or cyclic loading history disappeared after loading to higher load levels. This fact shows that neither creep strains, nor the residual strains that develop during cyclic loading, are a degradation phenomenon.
- Within the limit of the test conditions employed in the present study, residual strains that develop during cyclic loading were due essentially to the material viscous properties in addition to the development of irreversible strain increments by an increase in the inviscid load associated with cyclic loading, whereas the rate-independent effects of cyclic loading were negligible.
- The tensile load is basically a function of instantaneous irreversible strain and its rate in the case of monotonic loading. A non-linear three-component rheological model that has been validated for geosynthetic reinforcement subjected to monotonic loading conditions with and without intermediate sustained loading stages was extended to simulate the load–strain–time behaviour during cyclic loading. A proportional rule was used to describe the inviscid hysteretic load–strain relations. According to the model, the viscous load component under cyclic loading conditions could be linked to the inviscid load component by introducing another type of proportional rule to the inviscid load component. Without taking into account any rate-independent

cyclic loading effects in the model parameters, the model could simulate very well all the test results obtained from monotonic loading, sustained loading and cyclic loading tests.

## ACKNOWLEDGEMENTS

This study was supported by the Japan Society for the Promotion of Society through the grant: ‘Advanced application of soil reinforcement technology to highly earthquake-resistant reinforcement of existing soil structures and construction of highly earthquake-resistant and environment-friendly soil structures’. The authors are also grateful to T. Masuo and S. Ihara (Taiyo Kogyo Co. Ltd, Japan), T. Hirai (Mitsui Petrochemical Industrial Products Co. Ltd, Japan) and M. Ito (Maeda Kosen Co. Ltd, Japan) for providing the samples of geosynthetic reinforcement, and to K. Hara (Taiyo Kogyo Co. Ltd, Japan) for his advice in designing the gripping device.

## NOTATIONS

Basic SI units are given in parentheses.

- $a_i$  Coefficients of polynomial equation for  $V^f-\varepsilon^{ir}$  relation in simulations by the non-linear three-component model (dimensionless)
- $f$  inviscid tensile load: irreversible strain relation during primary monotonic loading (dimensionless)
- $g$  inviscid tensile load-irreversible strain relation during monotonic unloading (dimensionless)
- $g_v$  viscosity function of non-linear three-component model (dimensionless)
- $h_s$  loading history parameter (dimensionless)
- $m$  parameter of viscosity function (dimensionless)
- $n_R$  reloading scaling factor of the proportional rule (dimensionless)
- $n_U$  unloading scaling factor of proportional rule (dimensionless)

$\Delta t$	elapsed time (s)
$V$	tensile load (N/m)
$\Delta V$	cyclic load amplitude (N/m)
$V_0$	base tensile load of cyclic loading (N/m)
$V^f$	inviscid tensile load of non-linear three-component model (N/m)
$V^v$	viscous tensile load of non-linear three-component model (N/m)
$V_{iso}^v$	viscous tensile load of isotach type (N/m)
$\alpha$	parameter of viscosity function (dimensionless)
$\varepsilon$	tensile strain (dimensionless)
$\varepsilon^e$	elastic strain (dimensionless)
$\varepsilon^{ir}$	irreversible strain (dimensionless)
$\dot{\varepsilon}^{ir}$	irreversible strain rate ( $s^{-1}$ )
$\dot{\varepsilon}_r^{ir}$	parameter of viscosity function ( $s^{-1}$ )
$\varepsilon_{max}^{ir}$	previous maximum irreversible strain according to proportional rule (dimensionless)
$\varepsilon_{min}^{ir}$	previous minimum irreversible strain according to proportional rule (dimensionless)
$\Delta\varepsilon$	residual tensile strain (dimensionless)
$\sigma$	stress
$\sigma^v$	viscous stress of non-linear three-component model (Pa)
$\sigma^f$	inviscid stress of non-linear three-component model (Pa)

## REFERENCES

- Bathurst, R. J. & Alfaro, M. C. (1997). Review of seismic design, analysis and performance of geosynthetic reinforced walls, slopes and embankments. *Earth Reinforcement*, Ochiai et al., Editors, Balkema, Vol. 2, pp. 887–918.
- Bathurst, R. J. & Cai, Z. (1994). In-isolation cyclic load-extension behavior of two geogrids. *Geosynthetics International*, **1**, No. 1, 3–17.
- Christensen, R. M. (1981). Residual-strength determination in polymeric materials. *Journal of Rheology*, **25**, No. 4, 529–536.
- Christopher, B. C., Bonczkiewics, C. & Holtz, R. D. (1994). Design, construction and monitoring of full scale test of reinforced soil walls and slope. *Recent Case Histories of Permanent Geosynthetic-Reinforced Soil Retaining Walls*, Tatsuoka, F. & Leshchinsky, D., Editors, Balkema, pp. 45–60.
- Di Benedetto, H., Tatsuoka, F. & Ishihara, M. (2002). Time-dependent shear deformation characteristics of sand and their constitutive modelling. *Soils and Foundations*, **42**, No. 2, 1–22.
- Hirakawa, D., Uchimura, T., Shibata, Y. & Tatsuoka, F. (2002). Time-dependent deformation of geosynthetics and geosynthetic-reinforced soil structures. *Proceedings of the 7th International Conference on Geosynthetics*, Nice, Vol. 4, pp. 1427–1430.
- Hirakawa, D., Kongkitkul, W., Tatsuoka, F. & Uchimura, T. (2003). Time-dependent stress-strain behaviour due to viscous properties of geosynthetic reinforcement. *Geosynthetics International*, **10**, No. 6, 176–199.
- Kongkitkul, W., Hirakawa, D. & Tatsuoka, F. (2002a). Viscous deformation during cyclic loading of geosynthetics reinforcement. *Proceedings of the 7th International Conference on Geosynthetics*, Nice, Vol. 1, pp. 129–132.
- Kongkitkul, W., Hirakawa, D., Tatsuoka, F. & Uchimura, T. (2002b). Effects of viscous property on residual deformation of geogrid subjected to cyclic loading. *Proceedings of the 17th Geosynthetics Symposium (Japan Chapter of IGS)*, Tokyo, 159–166.
- Kongkitkul, W., Hirakawa, D., Uchimura, T. & Tatsuoka, F. (2004a). Loading rate effects due to viscous property on the strength and deformation property of geosynthetic reinforcement. *Proceedings of the 3rd European Geosynthetics Conference, EuroGeo3*, Munich, Vol. 2, pp. 533–538.
- Kongkitkul, W., Hirakawa, D., Uchimura, T. & Tatsuoka, F. (2004b). Residual deformation due to the viscous property during cyclic loading of geosynthetic reinforcement. *Proceedings of the 3rd Asian Regional Conference on Geosynthetics, GeoAsia 2004*, Seoul (submitted).
- Leshchinsky, D., Dechasakulsom, M., Kaliakin, V. N. & Ling, H.-I. (1997). Creep and stress relaxation of geogrids. *Geosynthetics International*, **4**, No. 5, 463–479.
- Ling, H. I., Mohri, Y. & Kawabata, T. (1998). Tensile properties of geogrids under cyclic loadings. *Journal of Geotechnical and Geoenvironmental Engineering, ASCE*, **124**, No. 8, 782–787.
- Min, Y., Leshchinsky, D., Ling, H.-I. & Kaliakin, V.N. (1995). Effects of sustained and repeated tensile loads on geogrid embedded in sand. *Geotechnical Testing Journal*, **18**, No. 2, 204–225.
- Moraci, N. & Montanelli, F. (1997). Behavior of geogrids under cyclic loads. *Proceedings of the Geosynthetic'97 Conf. California*, 2, pp. 996–976.
- Tatsuoka, F. & Leshchinsky, D. (1994). *Recent Case Histories of Permanent Geosynthetic-Reinforced Soil Retaining Walls, Proceedings of the Seiken Symposium*, Tokyo, No. 11, Balkema, Rotterdam.
- Tatsuoka, F., Tateyama, M. & Koseki, J. (1996). Performance of soil retaining walls for railway embankments. *Soils and Foundations*, Special Issue for the 1995 Hyogoken-Nambu Earthquake, 311–324.
- Tatsuoka, F., Tateyama, M., Uchimura, T. & Koseki, J. (1997). Geosynthetic-reinforced soil retaining walls as important permanent structures, 1996–1997 Mercer Lecture. *Geosynthetics International*, **4**, No. 2, 81–136.
- Tatsuoka, F., Koseki, J., Tateyama, M., Munaf, Y. & Horii, N. (1998). Seismic stability against high seismic loads of geosynthetic-reinforced soil retaining structures, Keynote Lecture. *Proceedings of the 6th International Conference on Geosynthetics*, Atlanta, Vol. 1, pp. 103–142.
- Tatsuoka, F., Ishihara, M., Di Benedetto, H. & Kuwano, R. (2002). Time-dependent shear deformation characteristics of geomaterials and their simulation. *Soils and Foundations*, **42**, No. 2, 106–132.
- Tatsuoka, F., Masuda, T. & Siddiquee, M. S. A. (2003). Modelling the stress-strain behaviour of sand in cyclic plane strain loading. *Journal of Geotechnical and Geoenvironmental Engineering, ASCE*, **129**, No. 6, 450–467.
- White, D. M. & Holtz, R. D. (1996). Performance of geosynthetic-reinforced slopes and walls during the Northridge, California earthquake of January 17, 1994. *Earth Reinforcement*, Ochiai et al., Editors, Balkema, Vol. 2, pp. 965–974.

The Editors welcome discussion in all papers published in *Geosynthetics International*. Please email your contribution to [discussion@geosynthetics-international.com](mailto:discussion@geosynthetics-international.com) by 15 September 2004.